

# On the validity of the Tada stress intensity factor solution for the single edge notch tension specimen with pinned ends

Zachary D. Harris<sup>1,2\*</sup>, Joseph W. Cochran<sup>3</sup>, Richard P. Gangloff<sup>d</sup>, Jacob D. Hochhalter<sup>3</sup>, and James T. Burns<sup>1</sup>

<sup>1</sup>Department of Materials Science and Engineering, University of Virginia, Charlottesville, VA

<sup>2</sup>Department of Mechanical Engineering & Materials Science, University of Pittsburgh, Pittsburgh, PA

<sup>3</sup>Department of Mechanical Engineering, University of Utah, Salt Lake City, UT

\*Corresponding author: zdh13@pitt.edu

---

## Abstract

The validity of the Tada stress intensity factor ( $K_{Tada}$ ) for pinned-ends single edge notch tension (SEN(T)) specimens is assessed via a combined experimental-modeling approach. Analysis of fatigue crack growth rate reductions during constant- $\Delta K_{Tada}$  loading demonstrates that specific combinations of alloy stiffness, geometry, and loading result in the true  $K$  deviating below  $K_{Tada}$ . Geometrically non-linear, 3-dimensional finite element calculations confirm mild-to-strong influences of these parameters, which are not captured by  $K_{Tada}$ . Most existing pinned SEN(T) data are found to use parameters where  $K_{Tada}$  is not significantly reduced, but the present results underscore the need for a more broadly applicable  $K$  solution.

## Highlights

- The validity of the  $K_{Tada}$  solution for the pinned SEN(T) is evaluated
- Measured  $da/dN$  reductions demonstrate that the true  $K$  can deviate below  $K_{Tada}$
- FE calculations quantify the influence of non-linear geometry effects on  $K_{Tada}$
- Most pinned SEN(T) data are valid due to low  $a/W$ , low  $K_{Tada}$ , and high alloy modulus
- A new  $K$  solution is needed to cover broader ranges of  $a/W$ , load, and alloy modulus

**Keywords** single edge notch, pinned SEN(T),  $K$  solution, fatigue crack growth, non-linear FEA

---

## 1. Introduction

The single edge notch tension [SEN(T)] specimen was originally proposed by Irwin, Krafft, and Sullivan as an alternative to the notched-round bar for plane strain fracture toughness testing [1–3]. While superseded in current fracture toughness standards [4,5] by the compact tension [C(T)] specimen [6], the SEN(T) is increasingly used to characterize the fracture toughness of reduced-constraint geometries, as well as fatigue crack growth and environment-assisted cracking (EAC) rates. For example, the similarity in the constraint profile of the SEN(T) geometry and an axially cracked pipe wall [7] motivated interest within the oil and gas industry to develop SEN(T)-based fracture toughness measurement standards [8,9].

Regarding EAC and fatigue crack growth testing, the increased use of SEN(T) specimens is driven by several factors. First, the specimen-cracked section is readily isolated in complex environments. Second, the SEN(T) geometry has rigorous-validated analytical relationships [10,11] for crack length measurement *via* the direct current potential difference (dcPD) technique [12,13], which provides automated input for programmed-stress intensity factor (K) loading. Third, the SEN(T) specimen enables studies pertinent to the so-called short/small crack problem in fatigue [14], particularly the role of environment [13,15]. In fact, SEN(T) measurements have elucidated: (a) the effect of short-crack size on the crack tip-chemical environment and associated fatigue crack growth rates (da/dN) [16], (b) transient and steady state da/dN changes in response to environment changes [17–21], (c) fatigue crack growth rates in the ultra-slow loading frequency, long hold time, and near-threshold K regimes where test duration is prohibitively long with the C(T) specimen [13,18,22,23], and (d) wide-range da/dN versus stress intensity range ( $\Delta K = K_{\max} - K_{\min}$ ) data for jet engine disk and blade fatigue life prediction [24,25]. The SEN(T) specimen has also been used to characterize crack size, metallurgical, and electrochemical effects on EAC under both sustained and monotonic loading [26–29]. This SEN(T) sample can yield accelerated growth rate data for fracture mechanics prognosis [30], and can incorporate an elastic-plastic J-integral capability [26]. However, broad applications of the SEN(T) specimen demand a validated K solution.

SEN(T) specimens are either threaded, clamped, or pinned into the load train, with each end-fixturing condition providing specific advantages. Both clamped and rigidly threaded SEN(T) specimens can be used for tension-compression fatigue experiments; the rigidly threaded condition is more convenient for high temperature testing [31,32]. While the pinned end-fixturing setup cannot be effectively used for reversed-load fatigue experiments, the same K is achieved with a significantly reduced applied load relative to the clamped condition [33]. The K solution for each end-fixturing condition also results in a unique sample geometry dependence. For example, the clamped SEN(T) K solution is sensitive to the ratio of the distance between the clamping lines (H) and the specimen width (W) [34], which has resulted in numerous proposed K solutions for specific ranges of H/W (reviewed by Zhu [33]). Conversely, the pinned and freely rotating SEN(T) geometry is reported to be insensitive to H/W for all  $H/W \geq 2$  (where H for rotating SEN(T) geometry is the distance between loading pin centers) [35,36], which led to widespread adoption of the K solution originally proposed by Tada et al. [35]:

$$K_{Tada} = \left( \frac{P}{BW} \right) \sqrt{\pi a} \left\{ \sqrt{\frac{2W}{\pi a} \tan\left(\frac{\pi a}{2W}\right)} \left[ \frac{0.752 + 2.02 \left(\frac{a}{W}\right) + 0.37 \left(1 - \sin\left(\frac{\pi a}{2W}\right)\right)^3}{\cos\left(\frac{\pi a}{2W}\right)} \right] \right\} \quad (\text{Eq. 1})$$

where  $P$  is the applied load,  $B$  is specimen thickness,  $W$  is specimen width, and  $a$  is crack length.

Historical studies of pinned SEN(T) specimens yielded reasonable agreement with Eq. 1, albeit with a notable exception for large  $H/W$ . Figures 1a and 1b compare the  $(a/W)$  dependencies of dimensionless  $K$ , and the difference in  $K$  from various authors relative to Eq. 1. Geometrically linear finite element calculations by Joyce *et al.* [37] and Tokuda and Yamamoto [36] were consistently within 1% of Eq. 1 for  $a/W$  up to 0.8. This excellent agreement was affirmed by a more recent linear finite element analysis of the pinned SEN(T) geometry with  $H/W$  of 20 by Hammond and Fawaz [38]. The pinned SEN(T)  $K$  solution determined by Gross *et al.* using the boundary collocation method was also consistently within 1% of Eq. 1 over the evaluated range of  $a/W$  from 0.05 to 0.50 [39]. Other studies reported dimensionless  $K$  versus  $a/W$  relationships that generally followed the trend of Eq. 1, but at somewhat lower dimensionless  $K$ . For example, a coupled experimental-computational study by Sanford and Kirk using the global collocation method informed by photoelastic fringe measurements exhibited a difference with Eq. 1 of between -1 and -5% for  $0.1 < a/W < 0.8$  [40]. Similarly, though only conducted over  $0.15 < a/W < 0.3$ , half-fringe photoelasticity measurements of Wang *et al.* indicated a consistent difference of -5% relative to Eq. 1 [41]. Finally, based on a mapping approach [42,43], Emery *et al.* reported differences from Eq. 1 ranging from -3 to -7% for  $0.1 < a/W < 0.62$  [44].

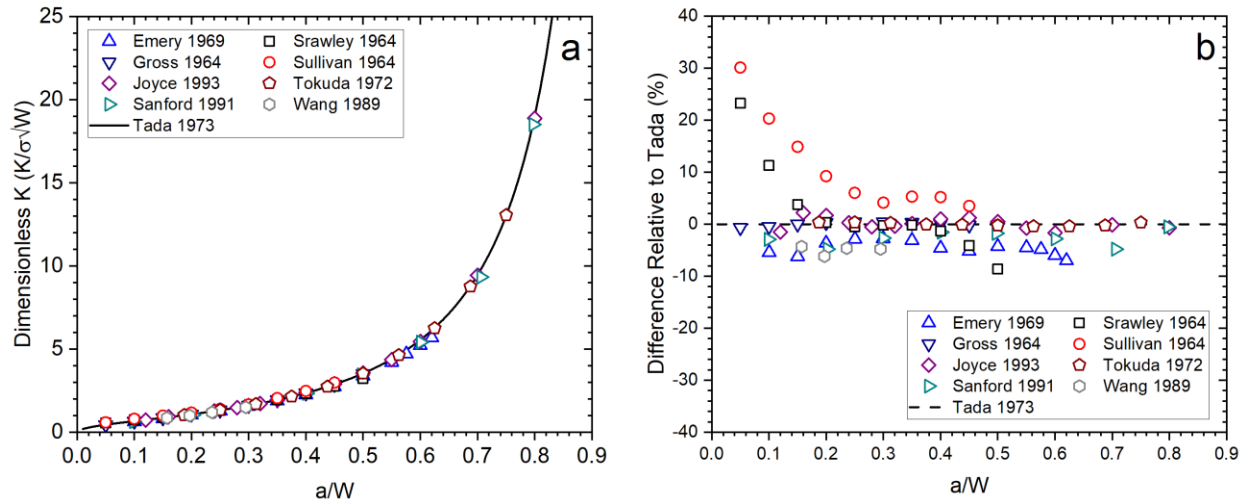


Figure 1 – Comparison of (a) dimensionless  $K$  and (b) difference relative to Equation 1 as a function of normalized crack length ( $a/W$ ) for literature  $K$  solutions of the pinned SEN(T) specimen geometry.

Older experimental studies generally agree with Eq. 1 over a somewhat limited range of  $a/W$ . Joyce *et al.* reported similar crack growth (R-curve) resistance behavior for pinned SEN(T) specimens of high strength steel with  $a/W$  ranging from 0.35 to 0.65, suggesting  $K$  solution (Eq. 1) accuracy for a case where

non-linear SEN(T) distortion could be in play [37]. Compliance measurements by Jack [45] on a pinned SEN(T) specimen agreed well with the predictions of Gross *et al.* for  $a/W$  up to 0.5 [39], suggesting concomitant agreement with Eq. 1. Dimensionless  $K$  from compliance measurements by Sullivan on AA7075-T6 generally disagree with Eq. 1 at low  $a/W$ , with a maximum difference of 30% at  $a/W = 0.05$ , but are within 5% difference for  $a/W$  between 0.3 and 0.5 [2]. Srawley *et al.* performed compliance measurements on AA7075-T6 SEN(T) specimens, which revealed large deviations from the results of Gross *et al.* (and therefore Eq. 1) [39] for  $a/W < 0.2$ . Srawley *et al.* recognized that these results are likely not valid due to the extreme challenge in measuring small opening displacements typical of this short crack regime [3]. Interestingly, at larger  $a/W$ , this study yielded good agreement with Gross *et al.* over the range  $0.2 < a/W < 0.4$ , but increasingly poor correspondence for  $a/W > 0.4$  (final measurement was at  $a/W = 0.5$ ) [3]. This deviation was attributed to the non-linear eccentricity that loading induced as the pinned SEN(T) geometry rotated open, particularly for longer crack lengths [3]. It was suggested that this yawing action could induce an  $H/W$  dependence into the  $K$  solution for the pin-loaded SEN(T) [3], as well as possibly reduce  $K$  below Eq. 1 due to loading pin friction [46].

An effect of  $H/W$  on the SEN(T)  $K$  solution is potentially important in studies of environment sensitive fatigue and EAC, as first recognized by Wei and coworkers [47]. They reported a steady 20 to 40% decrease in crack growth rate ( $da/dN$ ) with increasing  $a/W$  from 0.02 to 0.50 during constant stress intensity range ( $\Delta K_{Tada} = K_{max} - K_{min}$ ) loading of pinned SEN(T) specimens of AA2024-T3 in both dry  $O_2$  and aqueous NaCl. The  $da/dN$  decrease with increasing  $a/W$  was empirically associated with a decrease in the bracketed geometric term in Eq. 1 (*e.g.*, 0.8% decrease at  $a/W$  of 0.05, 1.5% at 0.10, 2.5% at 0.20, 4.0% at 0.30, 6.6% at 0.40, and 11.1% at 0.50). Following Srawley *et al.* [3], Wan *et al.* speculated that this was due to increasingly eccentric loading (and thus reduced net-section bending moment) as the fatigue crack grew in the rotating SEN(T) specimen [47]. Crack closure at the low-employed stress ratio ( $R=0.1$ ) may have caused part of this  $da/dN$  reduction, thus overstating the proposed adjustment to Eq. 1.

Extensive fatigue and EAC studies conducted in the 20 years after the work of Wei and coworkers support the accuracy of Eq. 1 for the pin-rotating SEN(T) specimen, at least for  $a/W$  in the range of 0.01 to 0.35 and relatively low employed  $K$  values. This work generally showed constant  $da/dN$  with increasing crack length during constant  $\Delta K_{Tada}$ -programmed loading using Eq. 1 [13,17–21,48,49]. Specific results reported for moderate to ultra-high strength steels and Al alloys are detailed in the Discussion. These experiments were designed to minimize growth rate-retarding crack closure and maintain a constant environment during crack growth at constant  $\Delta K$ . In all cases, the accuracy of Eq. 1 was supported for the pinned SEN(T) geometry with a reduced-section  $H/W$  that was high ( $\sim 10$ , and perhaps effectively of order 20) due to the tangs used to attach the SEN(T) specimen to clevises.

The validity of Eq. 1 recently again came into question based on fatigue experiments at constant  $\Delta K_{Tada}$ , supplemented by limited non-linear (geometry) finite element modeling of the pinned SEN(T) specimen with large H/W [50]. Dorman and Fawaz reported a steady reduction in  $da/dN$ , by 50%, with increasing  $a/W$  from 0.1 to 0.6 during constant  $\Delta K_{Tada}$  loading at constant stress ratio ( $R = 0.65$ ) using pinned SEN(T) specimens (reduced section  $W = 10$  mm and  $H/W = 10$  to 20) of AA7075-T651 stressed at a frequency of 1 Hz in laboratory air [50]. Dorman and Fawaz reported the same declining  $da/dN$  behavior for 40 fatigue experiments with SEN(T) specimens [51]: (a) taken from different locations in the thick plate, (b) fabricated by different shop methods, (c) with different notch dimensions, (d) with different pin sizes, (e) tested by different personnel, and (f) for an electrically isolated specimen in the dcPD circuit. By elimination, Dorman and Fawaz concluded that  $da/dN$  decreased with increasing  $a/W$  because  $\Delta K_{Tada}$  was under-predicted by Eq. 1 for large H/W due to the non-linear SEN(T) geometry influences [50]. To test this hypothesis, a single linear-elastic, non-linear geometry finite element calculation was conducted with the actual employed SEN(T) geometry [50]. The results of this calculation indicated that the true  $K$  for the tested aluminum alloy was 30% lower than that predicted from Eq. 1 at an  $a/W$  of 0.50. Such a result was notably higher than the empirically-based reduction in  $K$  of 11% estimated by Wan et al. for their testing geometry at  $a/W$  of 0.5 [47], suggesting a potential synergistic effect from loading, geometry, and alloy parameters.

This literature review establishes that: (1) the pinned-rotating SEN(T) specimen is an important tool in modern experimental studies of environment-sensitive fatigue and EAC, (2)  $K$  from many geometrically-linear finite element analyses are consistently within 1% of Eq. 1, and (3) a wide range of experimental studies using Eq. 1 yielded results that affirm this stress intensity solution, particularly at low-to-moderate  $a/W$ . However, results by Srawley *et al.* [3], Wei and coworkers [47], and Dorman and Fawaz [50] show that real  $K$  can be between 5% and 30% less than those given by Eq. 1. The magnitude of this deviation appears to increase with increasing SEN(T) H/W and  $a/W$ , as well as with decreasing load-train and specimen stiffness; factors that interact to increase the eccentricity of the load-line relative to the mid-point of uncracked net section [3]. Given the widespread use of the pinned SEN(T) specimen geometry (and therefore Eq. 1), both in past and on-going studies, this potential impact of such non-linear influences on  $K_{Tada}$  strongly motivate a detailed reexamination of Eq. 1 and its validity.

The objective of this study is to evaluate the accuracy of the elastic- $K_{Tada}$  solution (Eq. 1) for the pinned SEN(T) geometry, and to inform the direction of future modifications that account for non-linear geometry changes, via a combined experimental-computational approach. Constant  $\Delta K_{Tada}$  fatigue experiments are performed on Al, Ti, and Fe-based alloys to assess the evolution of  $da/dN$  as a function of  $a/W$ . The trends observed in these experimental data are compared to literature crack growth rate data. This

combined database is then interpreted using finite element simulation results, both geometrically linear and non-linear, conducted over a large SEN(T) geometry, uncracked ligament size, loading configuration, and material variable space.

## 2. Experimental Methods

### 2.1. Materials

Seven alloys were evaluated in this study, including: (1) 17-4PH stainless steel in the H1025 temper [52], (2) Custom 465 stainless steel in the H900 temper [53], (3) an experimental CrNiMoV martensitic steel [53], (4) 316L stainless steel in the cold-worked condition, (5) AA7075 in the T651 temper[54], (6) AA5456 in the H116 temper [55], and (7) Beta-C titanium in the solution-treated and aged (ST/A) condition [56]. Each alloy, except for 316L, was evaluated in prior studies by the authors; relevant material processing and sample extraction details, mechanical properties, and composition data are cited in the references above. 316L was procured as a cold worked 16-mm diameter bar. Supplier-reported yield strength was 545 MPa, ultimate tensile strength was 680 MPa, reduction in area was 69.1%, and composition (in wt.%) was 16.61% Cr, 10.55% Ni, 2.04% Mo, 1.32% Mn, 0.46% Cu, 0.31% Co, and 0.017% C, with the balance being Fe.

### 2.2. Fatigue crack growth experiments

For each material, SEN(T) specimens were extracted directly from the material stock; the flat-gage section width (W) and thickness (B), H/W ratio (where H is defined as the distance between the loading pins in the clevis configuration), initial notch length ( $a_0$ ), and specimen orientation for each alloy are summarized in Table 1. The X-Y sample orientation convention is used, where X is the material stock direction parallel to the loading axis and Y is the material direction parallel to the Mode I crack growth direction. For all materials, a starter notch with height of 38  $\mu\text{m}$  was introduced into each sample at the mid-height of the gage section using electrical discharge machining. The initial notch depth for each specimen was measured on each face of the gage section using a calibrated Hirox RH8800 digital microscope and then averaged to obtain  $a_0$ , while W and B were determined using digital calipers.

Fatigue crack growth experiments were performed on pin-loaded SEN(T) specimens using a servo-hydraulic mechanical load frame operated with Fracture Technology Associates FCGR software. The freely rotating end condition was met *via* clevis-based loading, where the SEN(T) specimen with threaded ends was screwed into tangs that were pin-fastened into clevises connected to very rigid load frame crosshead and actuator. The pins, clevises, and tangs were all machined from 17-4PH-H900. A schematic of the test configuration is shown in Figure 2.

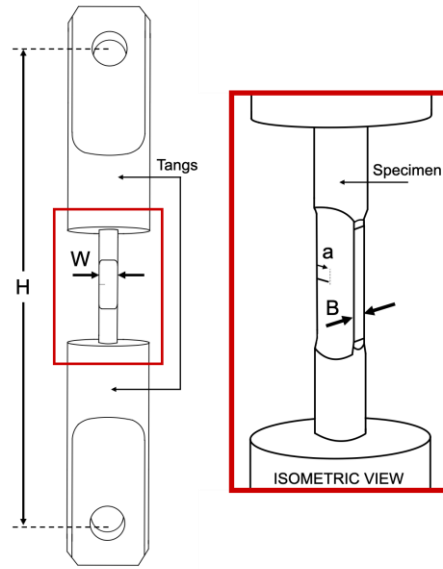


Figure 2 – SEN(T) specimen and model geometry with zoomed isometric view for detail.

After being placed in the mechanical load frame, each specimen was aligned with the clevises to allow for free rotation, in compliance with the boundary conditions of Eq. 1 [35]. All experiments were conducted in laboratory air at ambient temperature using a fixed stress ratio ( $R = K_{min}/K_{max}$ ), fixed  $\Delta K_{Tada}$  loading protocol, where the applied load was actively reduced based on continuous measurements of growing crack length. Details of the experiments are provided in Table 2.

Table 1 – SEN(T) geometry and orientation parameters for each tested alloy

Material	B (mm)	W (mm)	$a_0$ (mm)	H/W	Sample Orientation
17-4PH (H1025)	2.65	12.2	0.93	24	L-T
Custom 465-H900	2.65	10.2	0.2	29	L-R
CrNiMoV	2.65	10.2	0.2	29	N/A
AA5456-H116	6.60	17.25	1.5	14	S-T
AA7075-T651	2.65	10.1	0.2	29	L-T
316L (CW)	2.65	12.2	0.94	29	L-R
Beta-C (ST/A)	2.65	12.2	2.25	29	L-R

Table 2 – Overview of fatigue testing parameters for each alloy

Material	Precracking Protocol	Test $\Delta K$ (MPa $\sqrt{m}$ )	R	a/W Range
17-4PH (H1025)	Constant $\Delta K = 6.3$ MPa $\sqrt{m}$ at R = 0.1 from $a_0$ to 1.18 mm	9.0	0.5	0.1 to 0.8
Custom 465-H900	None; tested directly out of notch	10.0	0.65	0.1 to 0.85
CrNiMoV	None; tested directly out of notch	10.0	0.65	0.1 to 0.9
AA5456-H116	None; tested directly out of notch	5.0	0.5	0.1 to 0.8
AA7075-T651	None; tested directly out of notch	6.0	0.65	0.1 to 0.9
316L (CW)	Constant $\Delta K = 6.5$ MPa $\sqrt{m}$ at R = 0.1 from $a_0$ to 1.19 mm	7.0	0.7	0.15 to 0.75
Beta-C (ST/A)	Constant $\Delta K = 10.8$ MPa $\sqrt{m}$ at R = 0.1 from $a_0$ to 3.75 mm	15.0	0.5	~0.30 to 0.77

The subcritical growing crack length during each experiment was measured using the direct current potential difference (dcPD) technique [12,13] with a constant current (4.0 A for Fe-based alloys, 6.0 A for Al alloys, and 2.0 A for Ti alloys) applied through 10-gage copper wires attached to the 17-4PH tangs. Voltage measurements were taken using 36-gage alumel or copper wires (depending on the tested alloy; Al alloys used copper wire) that were spotwelded ~0.5 to 0.7 mm above and below the EDM notch. These voltage values were converted to crack length using Johnson's equation [10] where the adjustable constant ( $V_0$ ) was the potential associated with the initial notch length. Each potential measurement was corrected for thermally-induced voltages using current polarity reversal, with the average of approximately 500 individual voltage readings utilized per individual crack length measurement. The crack growth rate ( $da/dN$ ) was calculated from crack length versus cycle count data using the incremental ( $n=3$ ) polynomial method outlined in ASTM E647-15e1 [57]. Once the targeted-final a/W was reached, each specimen was fractured under displacement control.

### 2.3. Finite element modeling

Two finite element models were considered in this study. The first of these being the experimental test geometry detailed in Section 2.2, including tang grips and SEN(T) specimen; this model is referred to as the real SEN(T). The second model was an idealized dog bone specimen that captured the gauge region of the real SEN(T) specimen with similar pinned ends (Figure 3). This idealized geometry allowed multiple values of H/W to be readily assessed and enabled direct comparison to past research as this geometry is



more generalized. Three representative material systems were modeled: AA7075-T651, ST/A Beta-C Ti, and Inconel 718 with Young's moduli of 75, 100, and 200 GPa, respectively, to cover the full range of alloy stiffness.

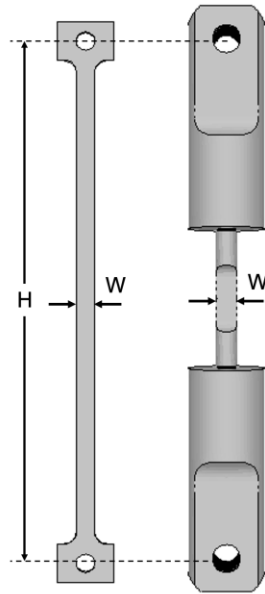


*Figure 3 - Idealized model geometry (left) and real SEN(T) model geometry (right).*

Initial (uncracked) SEN(T) geometries, boundary conditions, linear-elastic material properties, and geometrically linear or non-linear analysis of the 3D finite element models were defined in Abaqus [58]. Franc3D (F3D) was used to insert straight through cracks (analogous to previous 2D models) and compute  $K$  along the crack front using the M-Integral [59] with stress and strain fields computed by Abaqus. Franc3D works by inserting cracks that are entirely embedded within the geometry (i.e., not on an external face) so the full geometry was modeled without simplifying symmetries. Prior to inserting the crack, each model was subdivided into coherent global and local domains (Figure 4), which reduced remeshing to only the local model (i.e., only near the crack), while the global model mesh remained unchanged. This approach improved performance (via simplified remeshing steps) and provided improved control over mesh refinement near and coarsening away from the crack. The M-Integral method was used because it improves accuracy over alternatives such as displacement correlation or virtual crack closure methods [60]. Tada

likely employed a 2D finite element analysis that used weight function displacements to calculate  $K$ , leading to Eq. 1 [35].

Crack front elements were selected to be  $\frac{1}{4}$ -point wedge elements to model the stress singularity, which are surrounded by quadratic hexahedra (Figure 4) to form a crack front template that is used to improve the accuracy of the computed  $K$  values. Outside the crack front template, quadratic tetrahedra constituted the remainder of the local and global domains, see Figure 4. To mitigate any influence of numerical parameters on  $K$ , a convergence study identified the requisite mesh refinement and crack growth increments across the  $a/W$  domain. Convergence was determined to occur with a crack-front characteristic edge length of 0.125-0.5 mm, with approximately 20 quadratic elements through thickness, depending on the overall model size. The aspect ratio ( $H/W$ ) for the idealized models, where  $H$  is defined as the distance between pins, was modeled as 8, 16, and 29, whereas the true specimen geometry had an  $H/W$  of approximately 23. For all idealized model cases,  $a/W$  ranged from 0.1 to 0.9. For the true SEN(T),  $a/W$  ranged from 0.2-0.9.

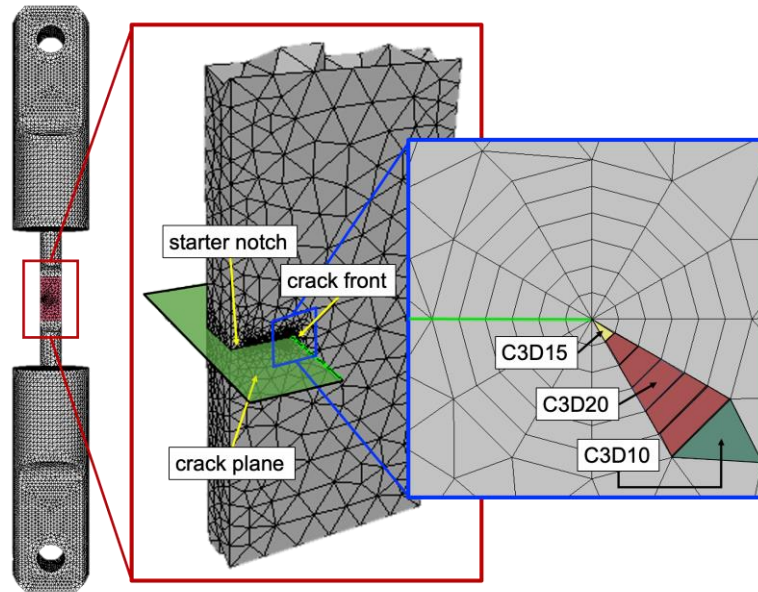


*Figure 4 – Global model for the real SEN(T), local model with an inserted crack, and a magnified view of the crack front template rosette with surrounding element annotations.*

The defined boundary conditions annotated in Figure 5 represent a frictionless pin-loaded coupon. Specifically, boundary conditions were defined at a reference point node at the pinhole center, which was then tied to a geometric surface or node-set. The reference point boundary condition included a vertically

applied load ( $P$ ) which remained vertical throughout the simulation. The specimen was free to rotate about the top and bottom pins ( $UR3$ ).

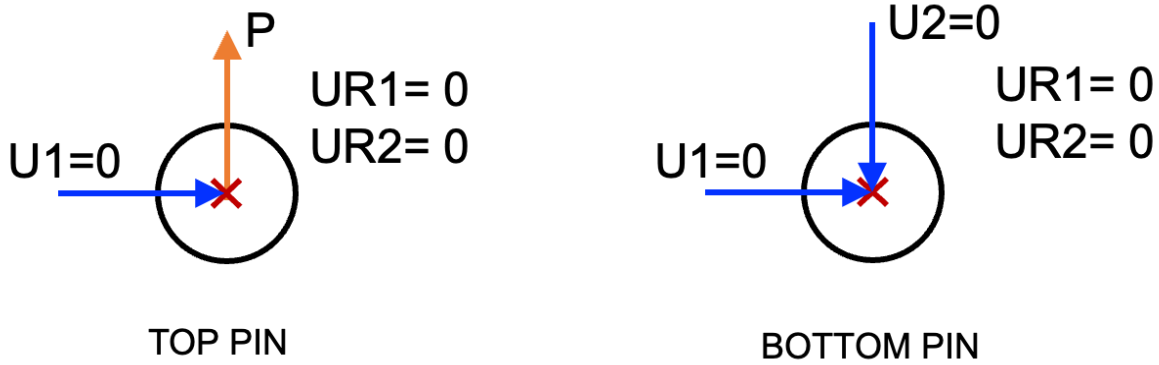


Figure 5 - Boundary conditions enforced for top (left) and bottom pins (right). Boundary conditions applied through reference points are depicted by red  $X$ 's.

### 3. Results

#### 3.1. Constant $\Delta K_{Tada}$ fatigue experiments

Measured fatigue crack growth rate versus  $a/W$  relationships for a CrMoNiV steel, Custom 465, 316L, and 17-4PH in the H1025 temper under various constant  $\Delta K_{Tada}$  and  $R$  are shown in Figure 6a-d, respectively. The four experiments broadly exhibit one of three behaviors. First, CrMoNiV (Figure 6a) loaded at  $\Delta K_{Tada} = 10 \text{ MPa}\sqrt{\text{m}}$  and  $R = 0.65$  exhibited constant  $da/dN$  over the range of tested  $a/W$ , with variations consistent with typical scatter in fatigue crack growth data [61,62]. Conversely, the 316L specimen loaded at a constant  $\Delta K_{Tada} = 7 \text{ MPa}\sqrt{\text{m}}$  and  $R = 0.7$  exhibits a continually decreasing  $da/dN$  over the tested  $a/W$  range (Figure 6d). Third, Custom 465 (Figure 6b) and 17-4PH (Figure 6d) exhibit constant  $da/dN$  up to  $a/W$  of 0.65 and 0.70, respectively, after which measured  $da/dN$  declines.

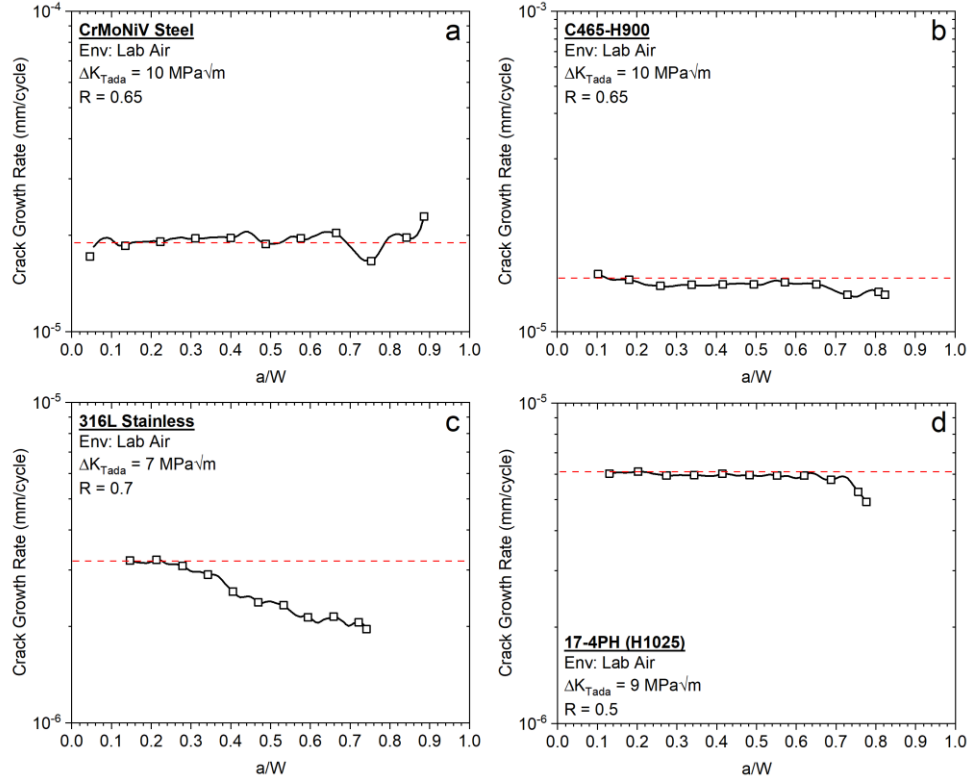


Figure 6 – Measured fatigue crack growth rate as a function of normalized crack length ( $a/W$ ) during constant  $\Delta K_{Tada}$  loading in laboratory air for SEN(T) specimens of (a) an experimental CrMoNiV alloy, (b) Custom 465, (c) cold-worked 316L, and (d) 17-4PH. The red dashed line corresponds to a constant  $da/dN$  as a function of  $a/W$ .

Similar crack growth rate variations were observed during constant  $\Delta K_{Tada}$  loading of AA7075-T651 and AA5456-H116, shown in Figures 7a and b, respectively. The AA7075 specimen tested at  $\Delta K_{Tada} = 6 \text{ MPa}\sqrt{\text{m}}$  and  $R = 0.65$  exhibited constant  $da/dN$ , with local variations and over a broad  $a/W$  range, followed by a sharp increase in  $da/dN$  as  $a/W$  approached 0.9. Speculatively, for very long crack depths, variability in the very low applied force ( $\sim 10$  to  $20 \text{ N}$ ) induced non-negligible errors in applied  $\Delta K_{Tada}$ , causing the accelerated  $da/dN$  in Figure 7a. The AA5456-H116 tested at  $\Delta K_{Tada} = 5 \text{ MPa}\sqrt{\text{m}}$  and  $R = 0.5$  exhibited mildly increasing  $da/dN$  over a large  $a/W$  range, as shown in Figure 6b. However, counter to AA7075-T651, AA5456-H116 exhibited a decrease in  $da/dN$  after  $a/W = 0.7$ , similar to the behavior noted for the 17-4PH steel in Figure 6d. Neither aluminum alloy exhibited steadily declining  $da/dN$  with increasing  $a/W$ , as reported by others [47,50,51].

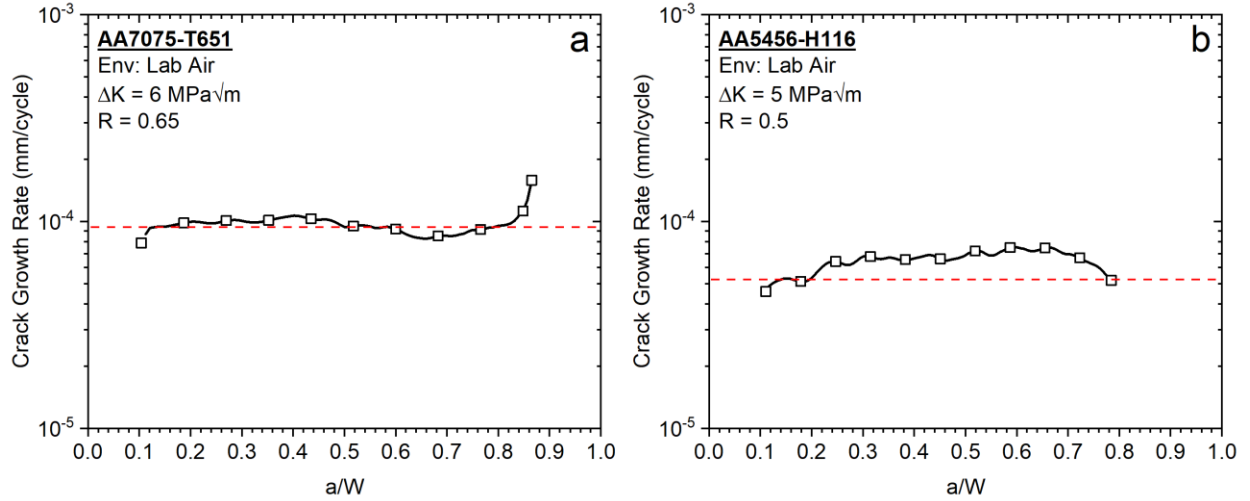


Figure 7 – Measured fatigue crack growth rate as a function of normalized crack length ( $a/W$ ) during constant  $\Delta K_{Tada}$  loading in laboratory air for SEN(T) specimens of (a) AA7075-T651 and (b) AA5456-H116. The red dashed line corresponds to a constant  $da/dN$  as a function of  $a/W$ .

An experiment conducted on ST/A Beta-C at constant  $\Delta K_{Tada} = 15 \text{ MPa}\sqrt{\text{m}}$  ( $R = 0.5$ ) exhibited a significant decline in  $da/dN$ . As shown in Figure 8,  $da/dN$  immediately begins to decrease as the experiment is initiated, followed by an inflection to an even steeper decline in  $da/dN$  at  $a/W > 0.6$ . In total,  $da/dN$  decreases by more than an order of magnitude, which is significantly larger than the deviations noted for the other experiments in this study (Figure 6 and 7), as well as those reported in the literature and summarized in the Discussion.

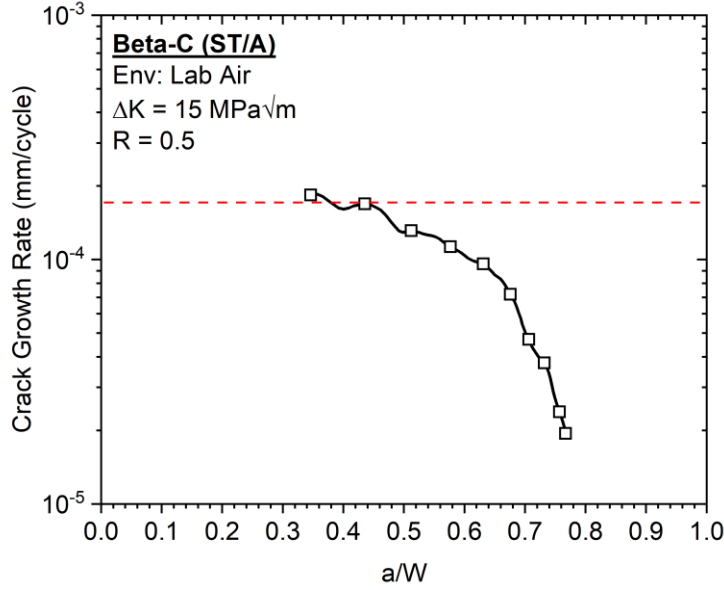


Figure 8 – Measured fatigue crack growth rate as a function of normalized crack length ( $a/W$ ) for a solution-treated and aged (ST/A) Beta-C titanium SEN(T) specimen in laboratory air loaded at  $R = 0.5$  and a constant  $\Delta K_{Tada} = 15 \text{ MPa}\sqrt{\text{m}}$ . The red dashed line corresponds to a constant  $da/dN$  as a function of  $a/W$ .

### 3.2. Finite element analysis

*Geometrically linear, plane-strain FEA* – to establish a comparative baseline between 3D FE results and Eq. 1 we impose plane-strain boundary conditions on the FE model for consistency with Tada's 2D plane-strain model. Plane-strain boundary conditions on the 3D model were imposed by constraining the z-displacement ( $U_3=0$ ) on front and back faces of the idealized specimen model. The results of this study are shown in Figure 9 for an  $H/W$  of 8, illustrating an average  $K_{FE}$  within  $\pm 1\%$  of  $K_{Tada}$ . The results are independent of  $H/W$ , so the consistency of  $K_{FE}$  and  $K_{Tada}$  persists for all  $H/W$ , so long as linear geometry with plane strain conditions is enforced in the FE model. In the following FE models studied, the plane-strain boundary conditions were not enforced, to model the crack front constraint more accurately, i.e., the 3D FE model does not require such an assumption.

*Geometrically linear FEA* – because of the focus on fatigue applications in this research we present results in terms of  $\Delta K$ , i.e.,  $K_{max} - K_{min}$ . To calculate the percent difference between  $\Delta K_{FE}$  and  $\Delta K_{Tada}$  we must assume the load ratio for simulation.  $R_{FE}$ , is equal to the load ratio obtained using Eq. 1,  $R_{Tada}$ . To align with experiment, a load ratio of 0.65 was used. The percent difference, Eq. 2, between  $\Delta K_{FE}$  and  $\Delta K_{Tada}$  are shown in Figures 10a-c and are observed to vary between 7-10%. The solid lines in Figure 10a-c illustrate the difference defined by Eq. 2 at the center of the crack front and shaded portions indicate the

variation in the computed  $\Delta K_{FE}$  along the 3D crack front. The percent difference is relatively insensitive to changes in  $a/W$  and is due to the removal of the plane-strain boundary condition in the 3D FE model. Essentially, this difference represents error in Eq. 1 from the plane-strain assumption. Additionally, the computed  $\Delta K_{FE}$  results are independent of load and  $H/W$ , which is consistent with the reviewed literature.

$$\text{difference relative to Tada (\%)} = \left( \frac{\Delta K_{FE} - \Delta K_{Tada}}{\Delta K_{Tada}} \right) * 100 \quad (\text{Eq 2.})$$

*Geometrically nonlinear FEA* – lastly, the difference between  $\Delta K_{FE}$  and  $\Delta K_{Tada}$  (for  $R=0.65$ ) with geometrically nonlinear FEA is illustrated in Figures 10d-f. As with Figure 10a-c, the solid lines in Figures 10d-f illustrate the difference defined by Eq. 2 at the center of the crack front and shaded portions indicate the variation in the computed  $\Delta K_{FE}$  along the 3D crack front. These results indicate a clear dependence of  $\Delta K_{FE}$  on  $P$ ,  $a/W$ , and  $H/W$ , which differs from previous geometrically-linear FE results and Tada (Eq. 1) [35–37]. Specifically, geometrically nonlinear FE results show that: (1) corresponding  $\Delta K_{FE}$  decrease sharply as  $a/W$  increases with respect to  $\Delta K_{Tada}$ , and (2) this effect is amplified with increases  $H/W$  or  $P$ .

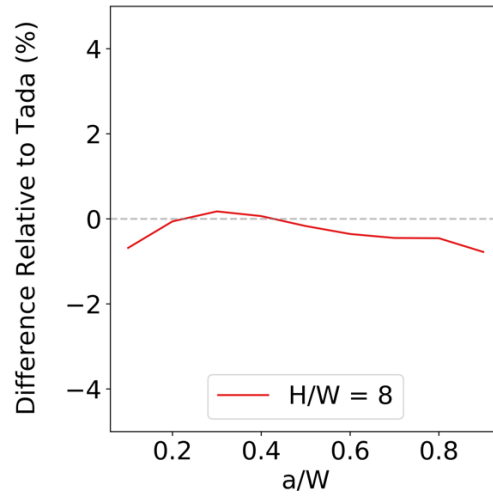


Figure 9 – Comparison of the difference relative to  $K_{Tada}$  as a function of normalized crack length ( $a/W$ ) for specimen geometry of  $h/W = 8$  and  $E=75$  GPa with added plane-strain boundary condition.

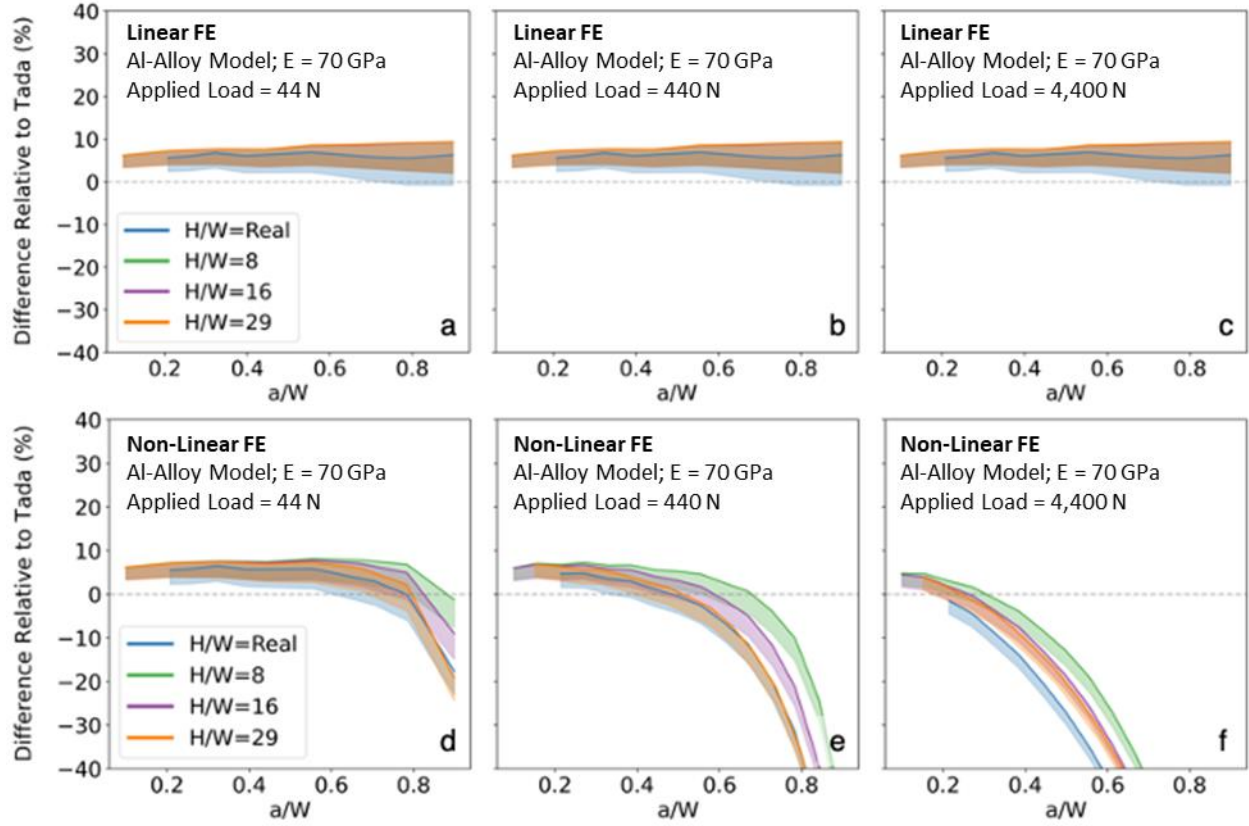


Figure 10 – Comparison of the difference relative to  $\Delta K_{Tada}$  ( $R=0.65$ ) as a function of  $a/W$ , load, and  $H/W$ . Linear FE is shown on the top row (a-c), and non-linear FE on the bottom row (d-f). The applied load is 44 N (a,d), 440 N (b,e), 4400 N (c,f), with an Al alloy model ( $E=70$  GPa).

Conventionally, stress intensity factors are a function of specimen geometry and loading, but not material properties [63]. However, the results in Figure 10 clearly indicate that the geometrically non-linear results increasingly differ from the idealized-linear  $\Delta K_{FE}$  (and Eq. 1) upon increased yawing (*i.e.*, increased  $a/W$ ,  $H/W$ , and  $P$ ). The geometrically linear finite element approximation overpredicts yawing and eccentric loading, as does Eq. 1 and the supporting models shown in Figure 1. Overpredicted yawing and eccentric loading result in higher-predicted  $\Delta K_{FE}$  values or, in other words, underpredicted load required to achieve a desired  $\Delta K_{Tada}$ . Since material stiffness influences the degree of yawing, it follows that an underlying  $\Delta K_{FE}$  dependence on material-elastic properties exists.

Consequently, any material-stiffness dependence of the computed  $K_{FE}$  was assessed using the geometrically non-linear FE analysis. To test this, the effect of elastic modulus ( $E$ ) varying ranging from 75 GPa (Al) to 200 GPa (Ni and Steel) was modeled with the real SEN(T) geometry because it is most pertinent for comparison to experimental results (Table 1 and Table 2). Note, for this comparison  $K_{FE}$  and  $K_{Tada}$  are explored (in lieu of  $\Delta K$ ) to directly assess percent differences in the SIF solutions. Consistent with



the experimental setup (Section 2.2), the threaded tang material was always 17-4PH in the H900 temper. Modeling the real geometry means that  $H/W$  remains fixed at the measured value, while  $a/W$  and load are varied. Non-linear FE simulations were completed, with loads ranging from 0.04 to 12.5 kN and  $a/W$  ranging from 0.1 to 0.9, producing a broad range of  $K_{FE}$  data points. Figure 11a-d illustrates a contour of this relative difference across the range of  $P$  and  $a/W$  values for each elastic modulus, 75 GPa (Figure 11a,c) and 200 GPa (Figure 11b,d). A cyan line indicates where the relative difference equals zero. The annotated white line on each of the contour plots represents an isoline of constant  $K_{Tada}$  with  $K_{Tada} = 17 \text{ MPa}\sqrt{m}$  in Figure 11a,b and  $K_{Tada} = 30 \text{ MPa}\sqrt{m}$  in Figure 11c,d. Finally, the relative difference along these white isolines is illustrated in Figure 11e-f. Comparing constant  $K$  values, the differences observed between the model results in Figure 11e (for 70 GPa) and 11f (for 200 GPa) demonstrate that there is an underlying  $\Delta K_{FE}$  dependence on material-elastic properties that is most potent at higher  $a/W$ .

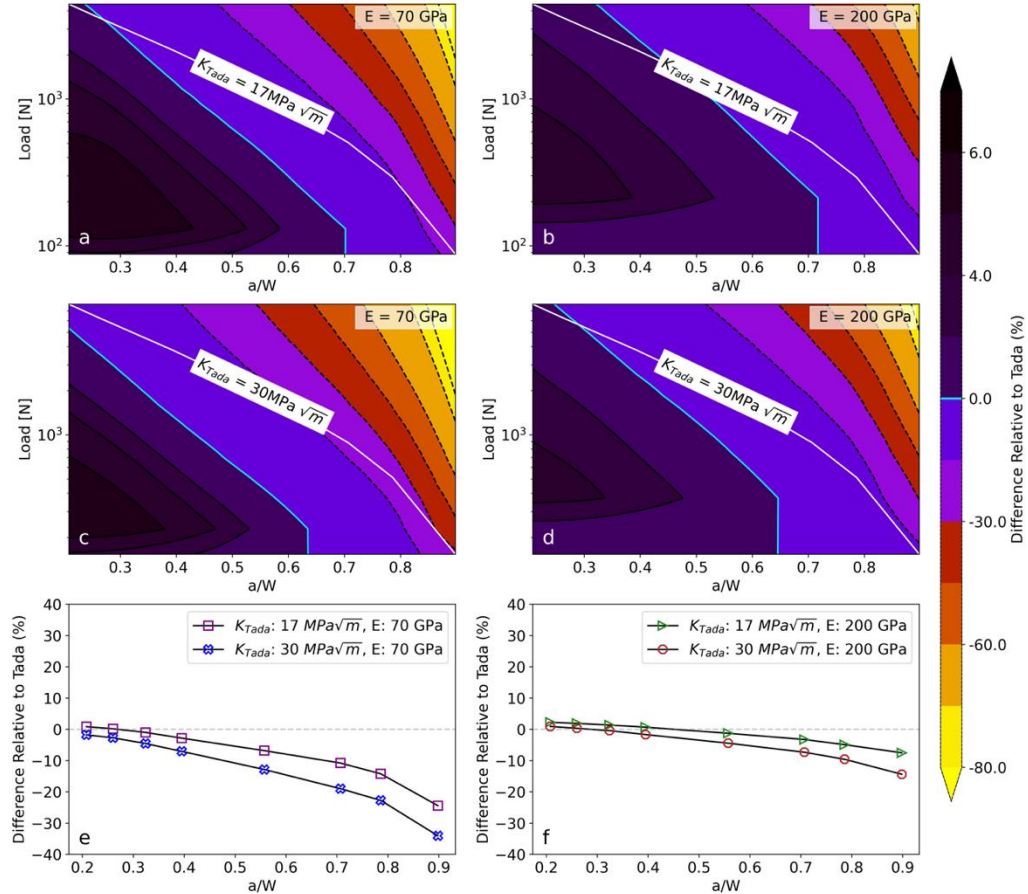


Figure 11 – Contours of the relative difference between  $K_{FE}$  from non-linear finite element analysis and  $K_{Tada}$  for the model based on the real SEN(T) geometry, as a function of  $a/W$  and load for the bounding material stiffness cases: Al (70 GPa, a and c) and Ni/Steel (200 GPa, b and d). The top row (a and b) corresponds to a  $K_{Tada} = 17 \text{ MPa}\sqrt{m}$ , while the middle row (c and d) corresponds to a  $K_{Tada} = 30 \text{ MPa}\sqrt{m}$ . The annotated white line shown in (a-d) represents the loads (predicted by Eq. 1) to maintain a constant

*driving force across  $a/W$ ; the cyan dashed line in (a-d) represents a relative difference of zero for visual references. The corresponding relative difference along the annotated white lines are plotted in e and f.*

## 4. Discussion

The preceding experimental and computational results demonstrate that material/geometry/loading combinations exist that result in Eq. 1 no longer being an accurate description of the K solution for the rotating SEN(T) coupon. Conversely, these results also reveal that there are combinations where Eq. 1 does accurately describe the K solution for the pinned SEN(T). The objective of the following discussion is three-fold: (1) compare the results observed herein to those reported in the literature from both a computational and experimental perspective, (2) leverage both the current results and prior reports to identify the factors governing the observed discrepancies between Eq. 1 and the true K, and (3) comment on the implications of observed findings, particularly regarding the validity of extensive EAC and environment-sensitive fatigue crack propagation data developed using the SEN(T) specimen.

### 4.1 Comparison with Literature FE Results

Reports of geometrically non-linear finite element modeling of the elastic K for the SEN(T) specimen is limited to the work of Galyon Dorman and Fawaz, who modeled the pin-loaded SEN(T) configuration using the material properties of AA7056-T651, large  $H/W$  of 20,  $a/W$  of 0.5, and  $K_{Tada}$  of  $17.1 \text{ MPa}\sqrt{\text{m}}$  [50]. The modeled  $K_{FE}$  from these calculations was 30% lower than that expected from  $K_{Tada}$ , yielding a relative difference (Eq. 2) of -0.30. This reported deviation is significantly larger than was observed for the same material, geometry, and loading conditions in the current study (Figure 10). Specifically, the current modeling exhibited a relative difference of -0.05 for AA7075-T651 at these  $a/W$  and  $K_{Tada}$  levels. In fact, even if a significantly higher  $K_{Tada}$  of  $30 \text{ MPa}\sqrt{\text{m}}$  (which is the upper bound of experimental relevance for this alloy) is used in the calculations (Figure 11), the observed difference at  $a/W = 0.5$  only rises to -0.11, still well below the -0.3 reported by Galyon Dorman and Fawaz [50].

The origins of the difference between the two calculations cannot be rigorously explored since the full details finite element modeling conducted by Galyon Dorman and Fawaz were not reported [50]. However, examination of a separate final report [51] written by these authors reveals reduced disagreement with the current calculations. Specifically, this report contains 13  $K_{FE}$  results (from both geometrically linear and non-linear calculations) for the same SEN(T) geometry and AA7075-T651 studied in the current manuscript. While the details of the modeling and the applied  $K_{Tada}$  were not provided, these additional calculations showed relative differences of +0.005 for  $0.2 < a/W < 0.5$ , -0.002 at  $a/W$  of 0.6, -0.01 at  $a/W$  of 0.7 and -0.04 at  $a/W$  of 0.8. Such results better align with the  $K = 17 \text{ MPa}\sqrt{\text{m}}$  results for AA7075-T651 in Figure 11 for  $a/W < 0.4$ , but do not fully capture the observed decrease in true  $K$  as  $a/W$  increases further. This suggests that a lower  $K_{Tada}$  than  $17 \text{ MPa}\sqrt{\text{m}}$  was employed for these simulations by Galyon Dorman and Fawaz, underscoring the  $K$  dependence on the extent of disagreement between Eq. 1 and true  $K$ .

## 4.2. Compilation of Fatigue Crack Growth Rate Data

Given the >60 years of use for the pinned SEN(T) geometry [2], substantial fatigue crack growth rate data exist to augment and compare with the current experiments. These data are summarized in Table 3, which documents the material, environment, applied-maximum  $K_{Tada}$ ,  $R$ ,  $H/W$  (defined in Figure 3), and observed- $da/dN$  trend for programmed-constant  $\Delta K_{Tada}$  loading per Eq. 1. For completeness, the current experiments from Figures 6-8 are summarized in Rows 12 through 18.

The first two rows of Table 3 list the literature results that have reported declining  $da/dN$  under programmed-constant  $\Delta K_{Tada}$  loading, which include the studies of Wei and coworker [47] as well as Galyon Dorman and Fawaz [50] that were summarized in depth in preceding sections. Rows 3 and 4 summarize the results of ~40 experiments performed by Galyon Dorman and Fawaz that broadly assessed the effect of fatigue protocol changes and crack closure retardation of  $da/dN$  for pinned SEN(T) specimens [51]. These results are notable as they reported steadily declining  $da/dN$  at programmed-constant  $\Delta K_{Tada} = 6 \text{ MPa}\sqrt{\text{m}}$  for all test conditions at  $R$  of 0.65 (Row 3), as well as for  $R$  of 0.8 and 0.1 (Row 4).

These reports of declining  $da/dN$  are contrasted by the historical studies performed by Gangloff and coworkers on both high strength steels and aluminum alloys, summarized in Rows 5-11 of Table 3. Considering the experiments performed on steels, the work reported in Row 5 revealed steady-constant  $da/dN$  for a 10-Ni steel with >1 GPa yield strength at 12 different  $\Delta K_{Tada}$  for  $a/W$  up to 0.3 and  $R = 0.1$  [13]. Critically, the magnitude of each measured  $da/dN$  agreed with data collected from C(T) specimens of the same steel, as reported by ~20 laboratories participating in an ASTM test program [62]. These same nominal findings of steady-constant  $da/dN$  were also noted for the experiments described in Rows 6 and 7, which

were performed on two high strength alloy steels in both  $H_2$  and hydrocarbon gas-mixture environments at  $R = 0.1$  from  $a/W$  of 0.01 to 0.1 [17].

Regarding Al alloys, Piascik and Gangloff noted constant  $da/dN$  for  $a/W$  of 0.02 to 0.35 for peak-aged AA2090 immersed in 1% NaCl solution at a fixed electrode potential for both low and high  $R$  (0.1 to 0.9) [18]. Similar results were also noted for peak-aged AA7075 by Ciccone, who performed constant  $\Delta K_{Tada}$  experiments in an aqueous solution simulating that in the lap joint of an aging commercial aircraft and observed steady-constant  $da/dN$  for  $a/W$  from 0.1 to 0.7 and across multiple replicate SEN(T) specimens [48]. However, some variability was reported in these results, with particular dependence on the testing solution employed. For example, Ciccone reported declining  $da/dN$  for 7055-T74511 under constant  $\Delta K_{Tada}$  loading in a modified lap joint simulated solution that promoted corrosion product formation. It was speculated in this study that this corrosion product was responsible for the observed decline via crack closure effects [48]. However, some variability (with isolated specimens exhibiting modest declines in  $da/dN$ ) was also observed for testing on AA7075-T651 in unmodified lap joint simulated solution, shown in Figure 12, which cannot be explained by corrosion product-induced closure.

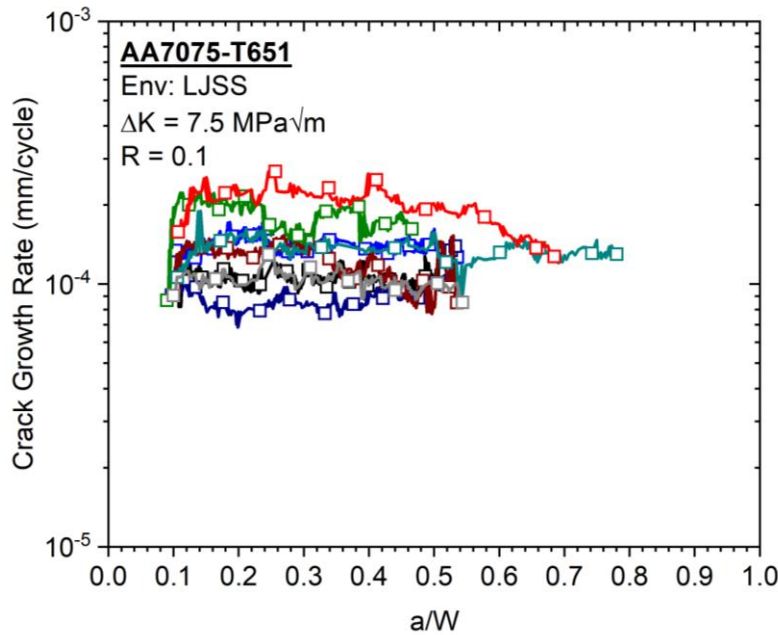


Figure 12 - Measured fatigue crack growth rate as a function of normalized crack length ( $a/W$ ) for eight duplicate AA7075-T651 SEN(T) specimens immersed in lap joint simulated solution (LJSS) loaded at  $R = 0.1$  and a constant  $\Delta K = 7.5 \text{ MPa}\sqrt{m}$ . Results extracted from Ciccone [48].

In total, the compilation of data presented in Table 3 implies four general  $da/dN$  versus  $a/W$  trends during constant-programmed  $\Delta K_{Tada}$  loading as prescribed by Eq. 1:

1. High strength, high modulus steels (Rows 5-8,12-13, 15 in Table 3) exhibit constant  $da/dN$  with increasing  $a/W$  over the tested ranges of  $\Delta K_{Tada}$ , geometry,  $R$ , and  $a/W$ .
2. Steadily decreasing  $da/dN$  with increasing  $a/W$  was noted for moderate strength stainless steel (Row 14) and a high strength titanium alloy (Row 18), and Al alloys (Rows 1 to 4, 10).
3. Transition behavior where a constant  $da/dN$  changed to steadily declining  $da/dN$  for two steels above a critical  $a/W$  of 0.65 to 0.7 (Rows 13 and 15) as well as for two Al alloys above a critical  $a/W$  of 0.7 to 0.8 (Rows 16 and 17).
4. Variable behavior, where both constant  $da/dN$  as well as steadily decreasing  $da/dN$  with increasing  $a/W$  occurs for replicate experiments of a single alloy, environment and loading level (Rows 9 and 11 and Figure 12).

*Table 3 – Summary of experimental  $da/dN$  changes during constant  $\Delta K_{Tada}$  loading of pinned SEN(T)s*

#	Authors	Material	Environment	Maximum $K_{Tada}$ (MPa $\sqrt{m}$ )	$R_{Tada}$	H/W	$a/W$	Growth Rate Response @ Constant $\Delta K_{Tada}$
1	Wan et al., 1996 [47]	AA2024-T3	Dry O <sub>2</sub>	5.6 11.1	0.1	2	0.02 to 0.5	Steady decrease in $da/dN$ by 20-40%
2	Dorman-Fawaz, 2019 [50]	AA7075-T651	Ambient-Humid Air	17.2	0.65	29	0.1 to 0.6	Steady decrease in $da/dN$ by 50%
3	Dorman et al., 2016 [51]	AA7075-T651	40 experiments as in [19]				0.1 to 0.6	Steady decrease in $da/dN$ by of order 50%
4	Dorman et al., Figure 13 [51]	AA7075-T651	Experiments at $R$ of 0.1, 0.65, 0.8 (maximum $K_{Tada}$ of 6.7, 17.1, 30 MPa $\sqrt{m}$ ) at $\Delta K_{Tada}$ of 6.0 MPa $\sqrt{m}$ [19]				0.1 to 0.6	Similar-steady decrease in $da/dN$ by of order 50%
5	Gangloff et al., 1992 [13]	10 Ni steel	Ambient Humid Air	5 to 40	0.1	~20	0.01 to 0.3	Constant $da/dN$ at 12 levels of constant $\Delta K_{Tada}$
6	Gangloff, 1988 [17]	4130 steel	UHV, H <sub>2</sub> , H <sub>2</sub> +C <sub>x</sub> H <sub>y</sub>	19.6	0.1	~10	0.02 to 0.1	Constant $da/dN$ at 4 different gas environments
7	Gangloff, 1988 [17]	4340 steel	UHV, H <sub>2</sub> , H <sub>2</sub> +C <sub>x</sub> H <sub>y</sub>	16.7	0.1	~10	0.01 to 0.1	Constant $da/dN$ at 4 different gas environments
8	Piasek-Gangloff, 1991 [18]	AA2090-T8	Aqueous NaCl	11 to 17	0.1 to 0.9	~20	0.02 to 0.35	Constant $da/dN$
9	Ciccone, 2005 [48]	AA7075-T6511	Aqueous LJSS	8.3	0.1	29	0.1 to 0.7	Constant $da/dN$
10	Ciccone, 2005 [48]	AA7055-T74511	Aqueous Modified LJSS	8.3	0.1	29	0.1 to 0.55	Steady decrease in $da/dN$ by factor of 3

11	Ciccione, 2005 [48]	AA7055-T74511	Aqueous LJSS	8.3	0.1	29	0.1 to 0.87	Constant da/dN
12	Figure 6a	CrNiMoV	Ambient-Humid Air	28.6	0.65	29	0.03 to 0.9	Constant da/dN; increase at a/W = 0.9
13	Figure 6b	Custom 465-H900	Ambient-Humid Air	28.6	0.65	29	0.1 to 0.82	Constant da/dN; decrease at a/W > 0.65
14	Figure 6c	316L	Ambient-Humid Air	23.3	0.7	29	0.14 to 0.74	Steady decrease in da/dN by 30%
15	Figure 6d	17-4PH H1025	Ambient-Humid Air	18	0.5	24	0.12 to 0.8	Constant da/dN; decrease at a/W > 0.7
16	Figure 7a	AA7075-T651	Ambient-Humid Air	17.2	0.65	29	0.08 to 0.9	Constant da/dN; increased at a/W > 0.8
17	Figure 7b	AA5456-H116	Ambient-Humid Air	10	0.5	14	0.1 to 0.80	Steady da/dN increase; decrease at a/W > 0.65
18	Figure 8	Beta-C (ST/A)	Ambient-Humid Air	30	0.5	29	0.33 to 0.76	Sharp-continuous decrease in da/dN by factor of 10

Examination of these overarching trends in Table 3 imply that for a sub-set of experiments the actual  $K$  may have deviated below  $K_{Tada}$  (Eq. 1). The extent of this stress intensity error varied with  $a/W$  and alloy modulus of elasticity for pin-loaded SEN(T) geometries similar to that in Figure 10. Since all crack lengths represented in Table 3, as well as in Figures 6 to 8, were within the stated applicable range of  $a/W$  up to 0.95 for  $K_{Tada}$  [35], it is reasonable to conclude that the non-linear geometric effect alluded to by Srawley et al. [3], Dorman and Fawaz [50,51], and Wan et al. [47] could be causing this behavior. However, several factors acting either on their own or in concert could also contribute to this behavior, including: (1) experimental variability, (2) crack closure, (3) large-scale crack tip plasticity, and/or (4) the applied boundary conditions not aligning with those assumed for  $K_{Tada}$ . The role of each listed factor is assessed in ensuing sections.

#### 4.3. Role of Experimental Variability and Inter-laboratory Differences

The majority of fatigue experiments in Table 3, including those from the present study, were performed with single SEN(T) specimens. Multiple fatigue crack growth experiments, conducted under nominally identical conditions, and employing a standardized specimen such as the C(T), typically lead to factors of 2 to 10 difference in  $da/dN$  at a given  $\Delta K$  [62,64]. This expectation is affirmed by the  $da/dN$  versus  $a/W$  data for eight constant  $\Delta K_{Tada}$  experiments on AA7075-T7651 in LJSS (Figure 12), which demonstrate that crack growth rates from test-to-test differed by up to 1.5-fold from the population mean, ranging from  $\sim 7 \times 10^{-5}$  to  $\sim 2.2 \times 10^{-4}$  mm/cycle [48]. The data in Figure 12 illustrates two classes of different  $da/dN$  versus  $a/W$  variations – those within a single experiment and from test-to-test – which are likely due

to subtle differences in microstructure, residual stress, specimen alignment, dcPD instrumentation, environment and perhaps other factors. Similar test-to-test variability is also noted in the data from 40 constant- $\Delta K_{Tada}$  experiments (Table 3, Row 3) conducted by Galyon Dorman and Fawaz [51].

While test-to-test variation in measured  $da/dN$  are important for conservative structural life prognosis and management, trends of either constant or decreasing  $da/dN$  are not well explained by any aspect of the test method that would be associated with test-to-test variability. The results of the many SEN(T) experiments carried by Galyon Dorman and Fawaz [51] support this assessment, as these experiments resulted in similar steady-declining  $da/dN$  with increasing  $a/W$  despite systematic variations in test method, alloy, and specimen machining details. However, there are notable exceptions to this assertion. As shown in Figure 12, replicate experiments with SEN(T) specimens of peak-aged AA7075-T651 [48] exhibited different  $da/dN$  versus  $a/W$  trends; the majority trend among eight-replicate tests was constant  $da/dN$  and the minority trend was steadily decreasing  $da/dN$ . Similarly, Galyon Dorman and Fawaz consistently reported steadily decreasing  $da/dN$  with rising  $a/W$  for AA7075-T651 (Table 3, Rows 3 and 4) [50,51], but Figure 7 shows nominally constant  $da/dN$  for  $0.08 < a/W < 0.8$ , followed by a decline in  $da/dN$  for  $a/W$  above 0.8 for this same alloy, applied  $\Delta K_{Tada}$ , and SEN(T) geometry/loading protocol.

The cause of these test-to-test variabilities in  $da/dN$  versus  $a/W$  trends (rather than  $da/dN$  magnitudes, as is often the focus) are not currently understood. While such behavior should certainly be explored further, a holistic assessment of the present results (Figures 6 to 8) and the summarized literature data in Table 3 strongly suggest that test-to-test variability cannot explain why: (1) for some alloys and loading conditions,  $da/dN$  is truly constant with increasing  $a/W$ , while (2) for other conditions, steadily decreasing  $da/dN$  under constant-programmed  $\Delta K_{Tada}$  is real. Factors that can cause such differences in behavior are now considered, particularly the role of alloy/loading specific crack closure, large-scale/net-section plasticity, and non-linear geometric changes.

#### 4.4. Role of Crack Closure

Fatigue crack wake closure occurs when the upper and lower faces of the crack wake come into contact during unloading and due to one or more mechanisms [65,66]; this reduces the effective mechanical driving force for fatigue crack growth ( $\Delta K$ ) if contact occurs before the applied-minimum load is reached. For example, the use of aqueous electrolyte testing in several experiments reported in Table 3 suggest that corrosion product and microstructure roughness-based mechanisms for closure could potentially be important. This arises from the fact that under constant  $\Delta K$  loading, the applied minimum and maximum loads each decrease as  $a/W$  increases. If the fatigue experiments are conducted at a low  $R$ , then the combination of a low applied force and continual reduction in force as  $a/W$  increases could result in the

progressive onset/increase of closure and concomitant-steady decrease in the effective  $\Delta K$ . This reduction in effective  $\Delta K$  manifests as either a progressively worsening decline in  $da/dN$  as  $a/W$  increased, or a constant  $da/dN$  that begins to trend downward above a critical  $a/W$  (when closure begins to occur).

Concerns related to a potential effect of crack closure are amplified by the reality that crack closure is very challenging to measure for the conditions represented in Table 3. As such, effective values of  $\Delta K_{Tada}$  versus  $a/W$  are not reported for any of the studies listed in Table 3, hindering direct quantification of the impact closure may be having. However, a holistic evaluation of Table 3 strongly suggests that closure is not an important cause of the observed reductions in measured  $da/dN$ . This view is justified by the fact that nearly all of the fatigue experiments used  $R$  values above 0.5, which typically limit closure effects. However, the most salient evidence for why the observed declining  $da/dN$  is unlikely due to crack closure is from the report of Galyon Dorman and Fawaz [51]. Specifically, for AA7075-T651 (Table 3, Row 4), continuously declining  $da/dN$  was observed in three experiments conducted at  $\Delta K$  of  $6.0 \text{ MPa}\sqrt{\text{m}}$  and  $R$  of 0.1, 0.65 and 0.8 [51]. In fact, the sharpest decline in  $da/dN$  was reported for the highest  $R$  of 0.8, which is opposite of expectations for a crack closure-driven behavior [66]. In addition to these fatigue experiment-based observations, it is also notable that similar reductions in applied  $K$  below  $K_{Tada}$  were also noted during the monotonic-loading compliance experiments conducted by Sullivan [2] as well as Srawley and coworkers [3]. Critically, such observations were noted under conditions where closure cannot possibly impact the applied  $K$ , strongly suggesting that other factors are responsible.

#### 4.5. Role of Large-Scale Crack Tip Plasticity

A second factor that could cause  $da/dN$  to deviate from a constant value during constant  $\Delta K_{Tada}$  loading is an  $a/W$ -dependent increase in the influence of plastic deformation on the crack tip field. If the applied load is sufficiently high, or the uncracked ligament is sufficiently small, then the assumptions of linear elastic fracture mechanics (LEFM) are no longer valid, resulting in increasing deviation between the real  $K$  and  $K_{Tada}$ . Given that many of the tested SEN(T) coupons listed in Table 3 have smaller width and thickness relative to other common specimen geometries (e.g., C(T) specimens [5]), it is possible that elastic-plastic fracture mechanics (EPFM) may be more applicable than Eq. 1. The fact that the observed declines in  $da/dN$  were mostly noted for the lowest strength steel and Al alloys in Table 3 supports an evaluation of the potential role of crack tip plasticity on the mechanical driving force.

To assess the possible contribution of crack tip plasticity, 3D finite element calculations of the calculated  $J$  as a function of  $a/W$  were performed under both linear elastic conditions (LEFM) and using the elasto-plastic (EPFM) material properties for AA7075-T651 [54]. The same geometry parameters and loading (maximum  $K_{Tada} = 17 \text{ MPa}\sqrt{\text{m}}$ ) as the experiment in Figure 11a were employed for this calculation.



For simplicity only and  $H/W = 29$  was simulated, as it represented the largest deviation. Note that this analysis can only be qualitatively related to the reported fatigue crack growth kinetics since  $J$  is not rigorously applicable to fatigue loading due to the assumption of no unloading in the original  $J$ -integral derivation [67,68]. EPFM simulations decompose total  $J$  integral into plastic ( $J_p$ ) elastic ( $J_e$ ) portions. The percentage of  $J_p$  is illustrated as a function of  $a/W$  in Figure 12, and reveals two key observations. First, the effect of plasticity on the real  $K$  is not negligible at low  $a/W$  for the tested material, geometry, and loading combination. Contributions of  $J_p$  range from 7% at  $a/W$  of 0.1 down to 3% at an  $a/W$  of 0.9. This change is both realistic and expected since the size of the monotonic plastic zone decreases in radius from 0.381 mm to 0.0167 mm due to the decreasing  $K$  as the crack propagated when loaded was applied per  $K_{Tada}$ . Second, some portion of  $J_p$  is present across the entirety of  $a/W$ . This finding leads to the question of if single parameter LEFM is valid or acceptable for this particular geometry and loading conditions. Additionally, the change in driving force due to plasticity follows the general trend (at a lesser magnitude) of the declining  $da/dN$  with increasing  $a/W$  behavior noted for the experiments summarized in Table 3. This suggests that plasticity may govern the declining  $da/dN$ , but additionally studies are needed to quantify what values of  $K$  and load would be affected.

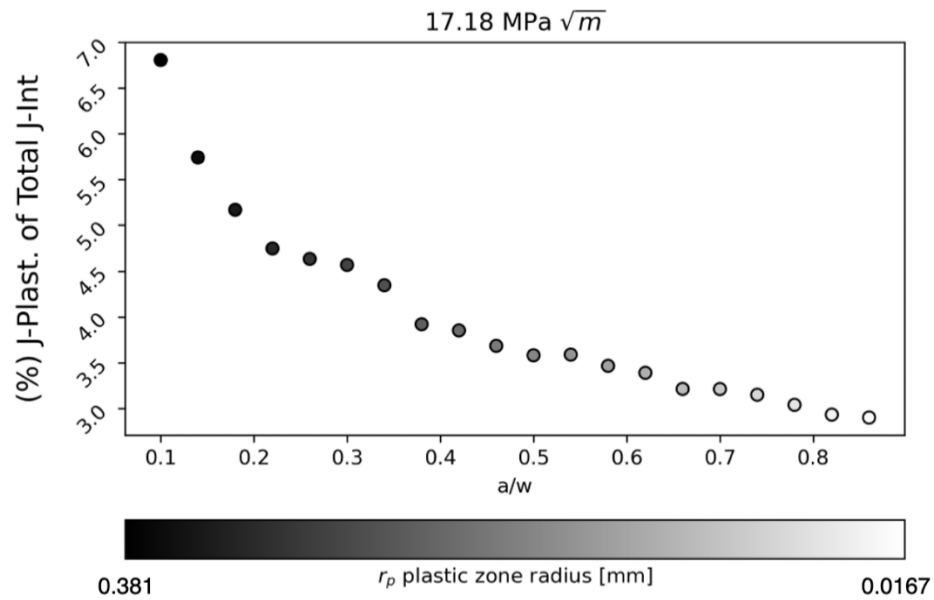


Figure 13 – Percent of  $J_p$  of total  $J$ -integral calculation from EPFM and LEFM as a function of normalized crack length for AA7075-T651 for constant  $K_{Tada} = 17 \text{ MPa}\sqrt{m}$ . The maximum plastic zone radius from measured from the crack tip is also included as a color bar.

#### 4.6. Role of Non-Linear Boundary Condition Change

The current finite element calculations presented in Figures 10 and 11 provide an opportunity for new insights on what is inducing the falling  $da/dN$  for constant-applied  $\Delta K_{Tada}$  loading. Specifically, these results establish that the computational methods used to derive  $K_{Tada}$  (Eq. 1) do not accurately describe the evolving boundary conditions for the pinned SEN(T) geometry over the  $a/W$  range up to 0.95 [35]. Note that this possibility has been previously reported by several authors. For example, it was argued that  $K_{Tada}$  does not accurately account for the changing-load eccentricity induced by the pinned SEN(T) yawing forward as the crack progresses [3,39,46,47]. Gross et al. speculated that this effect was responsible for the difference between linear boundary collocation calculations and compliance measurements on pinned SEN(T) specimens of AA7075-T6 [3,39]. Wan et al. proposed that the moment induced by such yawing, as well as a potential role of pin friction, as suggested originally by Pook [46], were responsible for decreasing  $da/dN$  vs.  $a/W$  during fatigue testing of AA2024-T3 SEN(T) specimens [47]. Others proposed that  $K_{Tada}$  does not account for the impact of geometry parameters (like  $H/W$ ) known to affect other SEN(T)  $K$  solutions that are sensitive to changes in loading-boundary conditions [6,69]. For example, Dorman and Fawaz concluded that the large-effective  $H/W$  of the AA7075-T651 pinned SEN(T) specimen and loading configuration caused declining  $da/dN$  during constant  $\Delta K_{Tada}$  loading [50].

This literature suggesting that  $K_{Tada}$  is inaccurate due to improper boundary conditions is inconsistent with experiments from both the current and prior studies (summarized in Table 3). In particular, fixed  $\Delta K_{Tada}$  experiments on seven high and ultra-high strength steels, as well as several high strength Al alloys all exhibited nominally constant  $da/dN$  over a broad range of  $a/W$ . Such fatigue-based results were augmented by the monotonic photoelasticity experiments of Sanford and Kirk on polycarbonate [40], which also exhibited good agreement with  $K_{Tada}$ . However, the current study also observed declining  $da/dN$  versus  $a/W$  relationships for Beta-C titanium (Figure 8) and 316L stainless steel (Figure 6c), consistent with the prior work suggesting errors in  $K_{Tada}$ . This dichotomy of experimental results, and the soundness of the many experiments represented in Table 3, therefore suggest a complex linkage between applied load, material, and sample geometry that is not adequately captured by  $K_{Tada}$ . Comparison of the linear and non-linear geometric finite element calculations in Figure 10 confirms this assessment. Specifically, the linear-geometric finite element calculations revealed good agreement with  $K_{Tada}$  for a range of applied forces and  $H/W$ . Such results are expected given (1) that this method was used by Tada to create this  $K$  solution [35] and (2) other studies using linear-geometric finite element calculations previously validated  $K_{Tada}$  [6,36–38]. Conversely, based on higher-order, non-linear geometric finite element calculations,  $K$  clearly deviates below  $K_{Tada}$ , with the amount dependent on applied load,  $a/W$ , geometry, and material stiffness, as demonstrated by Figures 10 and 11.

The difference between the geometrically linear and non-linear finite element results arises because the linear geometry assumption over-predicts the extent of yawing for the pinned SEN(T) geometry. This results in an under-prediction of the force necessary to achieve  $K_{Tada}$  for a given geometry and crack length, thus the calculated  $K_{Tada}$  from Eq. 1 is larger than the actual applied  $K$ . Moreover, since progressively larger displacements occur as the pinned SEN(T) increasingly yaws, this over-prediction of the applied  $K$  from linear-geometry FE becomes increasingly significant and motivates the need for a geometrically non-linear approach. However, the use of non-linear finite element analysis increases the sensitivity to factors such as the moment arm length (i.e.,  $H/W$ ), applied load, load train stiffness, and material stiffness. In fact, the non-linear geometry effect on the accuracy of  $K_{Tada}$  would be expected to increase as alloy-elastic modulus decreases,  $a/W$  increases, and/or applied load increases. Such effects are, in all cases, captured by the modeling presented in Figures 10 and 11, which confirmed the reduction in real crack tip  $K$  below the assumed applied  $K_{Tada}$  with decreasing modulus, increasing  $a/W$ , and increasing load. However, important differences were observed to be correlated with different material families, therefore the model predictions are best assessed by considering the fatigue data in Table 3, categorized by alloy stiffness.

#### 4.6.1 Steels

All fatigue experiments conducted on six different compositions of high and ultra-high strength steel (summarized in Table 3) showed effectively constant  $da/dN$  with increasing  $a/W$  at constant-applied  $\Delta K_{Tada}$  when  $a/W$  was less than 0.6. Constant  $da/dN$  in this regime is apparent in the published data [13,17,49] and the current experiments (Figure 6). This general observation is well-explained by the modeling shown in Figure 11. First, the maximum  $K_{Tada}$  during this fatigue experiments was always less than  $30 \text{ MPa}\sqrt{\text{m}}$  and often  $\sim 20 \text{ MPa}\sqrt{\text{m}}$ . Examination of Figure 11 demonstrates that the expected reduction in the true applied  $K$  relative to the assumed  $K_{Tada}$  for steels at  $a/W < 0.6$  is less than -5% at  $30 \text{ MPa}\sqrt{\text{m}}$  and -2% at  $20 \text{ MPa}\sqrt{\text{m}}$ . Such a reduction in  $K$  is sufficiently small that a tangible reduction in  $da/dN$  is unlikely to be observed, consistent with the noted constant  $da/dN$  versus  $a/W$  relationship for each high modulus steel. Second, the non-linear calculations in Figure 11 indicate that beyond  $a/W = 0.6$ , a steep reduction in the true applied  $K$  relative to the assumed  $K_{Tada}$  occurs, with the difference reaching between -5 to -15%, depending on the applied load and  $a/W$ . Such behavior is consistent with results in Figures 6b and 6d where, at fixed  $\Delta K_{Tada}$ ,  $da/dN$  decreases from the constant plateau when  $a/W$  exceeds 0.65 to 0.7 for 17-4PH and Custom 465 stainless steels. Interestingly, this falloff in  $da/dN$  at large  $a/W$  was not observed for the experiment on CrNiMoV (Figure 6a), where constant  $da/dN$  persists for  $a/W$  up to  $\sim 0.9$ . Speculatively, the small increase in the total- $K$  driving force due to increasing non-zero  $J_p$  contribution (on the order of 3% expected based on Figure 13) for these small uncracked-ligament sizes may offset the fall in crack tip driving force due to the non-linear boundary condition shift. However, why such an effect would only be

operative in the CrNiMoV steel, but not Custom 465 and 17-4PH, is unclear given that all are of similar ultra-high strength.

The lowest strength steel examined, 316L stainless steel, exhibited a steadily declining  $da/dN$  (reaching nearly 30% reduction) when stressed at constant  $\Delta K_{Tada}$ , which began at small  $a/W$  (Figure 6c). Such a result was surprising given that the applied maximum  $K_{Tada}$  for this experiment ( $\sim 23 \text{ MPa}\sqrt{\text{m}}$ ) was notably less than that used ( $\sim 28.5 \text{ MPa}\sqrt{\text{m}}$ ) during the testing on the other steels shown in Figure 6. It is speculated that this result may be due to the proximity of the employed  $\Delta K_{Tada}$  to the near-threshold regime for fatigue crack growth in 316L. For example, a 3% reduction in  $\Delta K$  from Eq. 1 would have significantly more impact as cracking moves from the Paris regime with a  $\Delta K^3$  dependence ( $1.03^3 = 1.09$ ) to the near-threshold regime with a  $\Delta K^8$  dependence ( $1.03^8 = 1.27$ ). Alternately, this behavior could be due to a residual stress distribution produced by the cold work used to manufacture this non-heat treated steel, in contrast to the higher strength quenched and tempered martensitic steels. Such residual stress could act to reduce the crack tip  $K$  further below both the assumed applied  $K_{Tada}$  and non-linear  $K_{FE}$ . An experiment with stress relieved 316L stainless steel, as well as replication of the single test result shown in Figure 6c and exploration of other  $\Delta K$  levels, would be useful to clarify this unexpected behavior.

#### 4.6.2. Aluminum Alloys

For lower elastic modulus aluminum alloys, the non-linear FE results in Figures 10 suggest a stronger decrease in the true applied  $K$  for a given assumed  $K_{Tada}$  compared to steel, and thus a stronger reduction in linear  $da/dN$  as  $a/W$  increases. For example, at  $a/W$  of 0.6, the non-linear  $K_{FE}$  is 7% and 14% less than  $K_{Tada}$  for applied  $K_{Tada}$  of  $17 \text{ MPa}\sqrt{\text{m}}$  and  $30 \text{ MPa}\sqrt{\text{m}}$ , respectively. This stronger non-linear influence is consistent with the fact that reduced  $da/dN$  was first reported as a problem for SEN(T) specimens of AA2024 and AA7075 (Table 3, Rows 1-4). Indeed, these 20% to 50% reductions in  $da/dN$  are consistent with a 7% reduction of  $\Delta K_{Tada}$  and the conventional  $da/dN$  dependence of  $\Delta K^{3-6}$  ( $1.07^{3-6} = 1.2$  to 1.5) for the Paris region.

While the experimental fatigue data in Table 3 for Al alloys generally support the predictions of the magnitude of non-linear boundary condition change effects on  $K_{Tada}$ , confirmation is somewhat ambiguous. For example, Ciccone did not observe a systematic  $da/dN$  reduction for AA7075-T651 (Table 3, Row 9) [48], while reductions in  $da/dN$  were observed for this alloy by Galyon Dorman and Fawaz [50]. This difference could be reasonably ascribed to the fact that Dorman and Fawaz consistently applied a higher  $K_{max}$  ( $17.2 \text{ MPa}\sqrt{\text{m}}$ ) compared to Ciccone ( $8.3 \text{ MPa}\sqrt{\text{m}}$ ), thus supporting the non-linear FE prediction of a load-level effect (Figure 10) and falling  $da/dN$ . Yet, this same  $K_{max}$  was used for testing in the current effort (Figure 7a) on the same alloy and was not observed to induce a sustained decline in  $da/dN$ . Such

ambiguity is further underscored by the results of Ciccone on AA7055-T7451 [48], where samples tested under constant  $\Delta K_{Tada}$  loading either exhibited declining or constant  $da/dN$ , and that of Piascik and Gangloff on AA2090 (Table 3, Row 8), who observed constant  $da/dN$  for a wide range of applied-constant  $\Delta K_{Tada}$  and  $K_{max}$ , albeit over a limited  $a/W$  window up to 0.35 [18]. While the sum of the experimental and computational work support an increased error in  $K_{Tada}$  for aluminum alloys, this strong variation in the magnitude of the non-linear geometry effect from study-to-study (or even within a single study) merits further exploration to understand the source of these ambiguities.

#### 4.6.3 Titanium Alloys

Titanium alloys of intermediate-elastic modulus ( $\sim 100$  GPa) compared to steel and Al alloys should exhibit reductions of  $K_{Tada}$  intermediate to those modeled in Figure 10. While only a single SEN(T)-based fatigue experiment is available for high strength (body-centered cubic) titanium alloys, this result (Figure 8) revealed that  $da/dN$  at constant  $\Delta K_{Tada}$  ( $K_{max} = 30 \text{ MPa}\sqrt{\text{m}}$ ) decreases by an order of magnitude as  $a/W$  rises from 0.3 to 0.75. This decrease is much larger than those observed for steels and Al alloys (Table 3) and is much greater than expected based on the non-linear FE results in Figure 10. The cause of this strong reduction in  $da/dN$  is not fully understood, but is notable that a significant portion of the decrease in  $da/dN$  occurs over  $a/W$  from 0.65 to 0.75, consistent with the onset of sharply increasing error in applied  $K$  reported in Figure 10. Speculatively, the reduction in true applied  $K$  may be sufficiently large that the near-threshold regime is being approached (resulting in a sharper decline in  $da/dN$ ), but additional experiments are necessary to confirm this possibility. However, the pinned SEN(T) specimen was successfully used to characterize the  $da/dN$  behavior of Ti-6V-4Al, so long as  $a/W < 0.6$ , paralleling the details considered in the next section for Ni-based superalloys [70].

#### 4.6.4 Ni-based Superalloys

Since Ni-based superalloys exhibit elastic moduli similar to steel, this class of alloys should exhibit small reductions in the true crack tip  $K$ , compared to  $K_{Tada}$ . However, to the authors' knowledge, there are no published data of  $da/dN$  versus  $a/W$  at programmed-constant  $\Delta K_{Tada}$  for pinned SEN(T) specimens to test this expectation. That being said, Van Stone and coworkers successfully applied the small pin-loaded SEN(T) specimen with programmed-declining  $\Delta K_{Tada}$  to establish  $da/dN$  in the near threshold regime for high strength Ni superalloys (e.g., Rene 95 and PWA 1484) [24,25]. Note that these specimens were small; thickness = 2.5 mm,  $W = 10$  mm and  $H/W = 6.5$  [70]. At threshold crack 'arrest', the applied load range was fixed at a somewhat higher value and  $\Delta K_{Tada}$  increased with subsequent crack growth to a maximum  $K_{Tada}$  of 40-55  $\text{MPa}\sqrt{\text{m}}$ . Measured  $da/dN$  values were well aligned with extensive data obtained from surface crack specimens that were optimized for accuracy [13,24,25]. Unpublished-proprietary studies with a variety of Ni superalloys used the SEN(T) and Eq.1 to produce  $da/dN$  data that agreed with surface-crack

growth rates so long as the SEN(T)  $a/W$  was  $< 0.6$  and net section stress (simply load/uncracked ligament area) was  $< 75\%$  of alloy yield strength [70]. Figure 10 shows that  $K$  from the 3-D geometrically non-linear FE model is only 4-5% less than  $K_{Tada}$  for applied  $K$  of  $30 \text{ MPa}\sqrt{\text{m}}$  and an alloy modulus of 200 GPa, with very large  $H/W$  of 23. Smaller differences, extending to higher  $a/W$  or higher  $K_{Tada}$ , are predicted for  $H/W$  of 6-8. As such, these FE model predictions are consistent with this laboratory experience for Ni-based alloys, which further affirms the validity and broad applicability of  $K_{Tada}$  given by Eq. 1 for the alloy,  $a/W$ ,  $H/W$  and stress intensity bounds given by the non-linear FE results in Figures 9 and 10.

#### 4.6.5 Other Comparisons with Experiment

Compliance and photo elastic measurements of the SEN(T) geometry are limited; however, those reported are consistent with the non-linear FE assessment of reductions from  $K_{Tada}$  represented in Figures 9 and 10. The influence of load magnitude explains why Sanford and Kirk [40] observed excellent agreement between experimentally determined  $K$  and  $K_{Tada}$  for the SEN(T) specimen, despite using a compliant material (polycarbonate) for their experiments. While the exact loading conditions were not reported, the low toughness of polycarbonate ( $< 5 \text{ MPa}\sqrt{\text{m}}$ ) would necessitate these authors to employ a low  $K$  in their photoelastic experiments. Decreasing  $H/W$  reduces the non-linear geometric influence on  $K$ . This explains why the compliance measurements of Srawley et al. [3] on AA7075-T6 ( $H/W$  of  $\sim 3.3$ ), presented in Figure 1b, reasonably agree with  $K_{Tada}$  over the same range of  $a/W$  where the calculations in Figure 10a ( $H/W = 29$ ) reveal increasing relative difference due to specimen yawing.

### 4.7. Implications and suggested future research directions

There are two overarching implications from the current study. First, comparison of experiment and modeling establishes that the  $K_{Tada}$  solution for the pinned SEN(T) geometry (Eq. 1) loses high accuracy only for specific combinations of specimen geometry, material stiffness, and applied loading. Potential error in  $K_{Tada}$  was suggested by others due to changing boundary condition and loading eccentricity during crack growth, but the effects were not quantified in those studies [47,50]. The current study demonstrates that the reduction of applied  $K$  compared to  $K_{Tada}$  arises from a complex non-linear geometry influence, and defines regimes of alloy stiffness, load, and untracked ligament size where these errors become significant. This finding contrasts with the stated broad accuracy of  $K_{Tada}$   $0.05 < a/W < 0.95$  [35–38,40]. However, these prior studies did not capture non-linear geometry effects. For example, the experimental validation by Sanford and Kirk utilized very low  $K$  loading [40], while modeling of Joyce and others used geometrically linear finite element approaches [34,36,37], which inherently neglect such effects.

As called for by others [47,50], it is necessary to develop a new  $K$  solution that can be broadly employed for pinned SEN(T) samples of different alloy stiffness and loading configuration by accounting for the influence of non-linear geometry change. Recently developed machine learning-based, genetic

programming algorithms [71] were shown to be effective for developing straight-forward  $K$  solutions that accurately capture complex dependencies; such approaches can be leveraged for the pinned SEN(T). Moreover, geometrically non-linear FE modeling should be employed to assess the extent to which boundary conditions changes affect accepted  $K$  solutions for other bending-based specimens such as the C(T) and eccentrically loaded single edge notch tension (ESE(T)) geometries employed in fatigue and EAC studies [72].

The second implication of this study is that there are clear combinations of material stiffness, specimen geometry, and loading that result in true  $K$  values that agree within 5% or better with  $K_{Tada}$ . For example, the non-linear finite element simulations show that  $K_{Tada}$  is within 5% of the calculated  $K$  value up to  $a/W = 0.6$  for a realistic pinned SEN(T) specimen configuration ( $H/W = 29$ ) loaded to  $K_{max} = 17$  MPa $\sqrt{m}$  for Al alloys (Figure 10). For stiffer steels, this critical  $a/W$  is 0.75 for this  $K$  level and 0.6 for higher  $K$  of 30 MPa $\sqrt{m}$ . Nickel-based superalloys will likely align with this regime of validity established for steel, while Ti alloys will be intermediate to steel and Al alloys. This assessment is affirmed by the extensive fatigue crack growth data sets summarized in Table 3 and the compliance results of Srawley and Gross (Figure 1b) [3,39].

The present results strongly support the conclusion that historical fatigue and EAC data developed using pinned SEN(T) specimens are overwhelmingly valid [13,17–21,26,27,48,52–55,61,62,73–83]. Nearly all these experiments were performed at  $a/W < 0.4$ , with many conducted at  $a/W$  of 0.1 or less, where non-linear geometry effects are minimal. Moreover, the threshold stress intensity ( $K_{TH}$ ) where EAC initiates is generally  $< 20$  MPa $\sqrt{m}$  for nickel alloys/steels and  $< 10$  MPa $\sqrt{m}$  for Al alloys, leaving an appreciable range over which  $K_{Tada}$  and therefore measured crack growth rate ( $da/dt$ ) vs.  $K$  relationships are valid. Nonetheless, it is likely that non-negligible errors are present in the high- $K_{Tada}$  portion of those SEN(T)-based datasets that exceed  $\sim 80$  MPa $\sqrt{m}$  for high modulus steels and Ni alloys [28,75,76,79]; additional studies are needed to quantify the error in applied  $K$  for these experiments. As suggested by Figure 12, large scale plasticity elevates the true crack tip  $K$  above the elastic  $K_{Tada}$  and  $K_{FE}$ . This contribution may be important for such high  $K$  levels and lower-strength alloys.

Future work should focus on understanding these effects for existing datasets, but also more generally on defining the expected error across the entire range of geometry, load, and material combinations for scenarios where using  $K_{Tada}$  is required (as may be the case for preprogramed control software systems). Such information could then be used to modify the specimen geometry design to maximize the usable  $a/W$  where  $K_{Tada}$  remains valid. Conversely, if a certain test geometry is dictated by material availability or other reasons, then (1) non-linear finite element simulations can be performed to

determine the validity bounds of  $K_{Tada}$  for that specific geometry and/or (2) an experimental validation (akin to data in Figures 6-8) could be conducted to explore the maximum  $a/W$  that results in constant growth kinetics.

## 5. Conclusions

The efficacy of the elastic solution for  $K_{Tada}$  for the pinned-rotating SEN(T) geometry was assessed via a combined approach that leveraged extensive-constant  $\Delta K$  fatigue experiments and targeted finite element modeling simulations. From these data, the following conclusions are established:

1. Depending on the combination of the pin-loaded SEN(T) geometry (particularly  $H/W$ ), alloy modulus, uncracked ligament size, and applied stress intensity, constant  $\Delta K_{Tada}$  experiments exhibit either broadly constant, progressively decreasing, or constant-to-decreasing forms of  $da/dN$  vs.  $a/W$  at constant-applied  $\Delta K_{Tada}$ .
2. These experimental trends suggest that the true  $K$  for the pinned SEN(T) geometry either equals or is less than  $K_{Tada}$ ; this deviation is not constant and increases with those factors that promote increasing ‘yawing’ changes in the geometric boundary conditions of the SEN(T).
3. The existing solution for  $K_{Tada}$  was reproduced for a wide range of  $a/W$ , consistent with previous models, if linear geometric simulations are performed with constant boundary conditions. However, 3-D non-linear geometric finite element analysis establishes significant deviations from  $K_{Tada}$ .
4. Non-linear finite element modeling shows that yawing open inherent to the pinned SEN(T) geometry causes the true  $K$  to increasingly deviate below  $K_{Tada}$  as crack length increases, but only above a critical  $a/W$ ; modeling confirms that the amount of reduction increases with increasing pin spacing, decreasing uncracked ligament size, decreasing alloy stiffness, and increasing load for large  $H/W$  loading.
5. Experimentally observed reductions in measured  $da/dN$  at constant  $\Delta K_{Tada}$  cannot be convincingly attributed to crack-wake closure or crack tip plasticity. Rather, occurrences of constant as well as declining and transition  $da/dN$  vs.  $a/W$  at constant  $\Delta K_{Tada}$  are most consistently explained by the non-linear geometry influence not accounted for in  $K_{Tada}$ .
6. Most existing fatigue and EAC datasets based on pinned SEN(T) specimens are accurate because test conditions reside in regions of  $a/W$ , alloy stiffness, and applied loading where the true  $K$  is reasonably described by  $K_{Tada}$  (e.g., at critical  $a/W < 0.6$  to  $0.75$  for Al alloys and steels,



respectively, at relevant applied  $K$ ). However, experimental cracking data collected at high  $K_{Tada}$ , or at larger  $a/W$ , will require non-linear FE correction of  $K_{Tada}$ .

7. A  $K$  solution should be developed for the pinned SEN(T) geometry to replace  $K_{Tada}$  that incorporates this influence of non-linear geometry effects, such as  $H/W$ .

## 6. Acknowledgements

Helpful discussions with Dr. Brian Somerday and Dr. Kevin Nibur as well as support and resources from the Center for High Performance Computing at the University of Utah are gratefully acknowledged. This research was financially supported by the National Aeronautics and Space Administration (NASA) through the NASA Engineering & Safety Center under Award #80NSSC21P0569 with Heather Hickman as Program Manager.

## 7. Data Availability Statement

The raw and processed data generated during this study will be made available upon reasonable request.

## 8. References

- [1] Srawley JE, Brown W. Fracture Toughness Testing Methods. Fracture Toughness Testing and its Applications, West Conshohocken, PA: ASTM International; 1965, p. 133–98. <https://doi.org/10.1520/STP26588S>.
- [2] Sullivan AM. New specimen design for plane-strain fracture toughness tests. Materials Research and Standards 1964;4:20–4.
- [3] Srawley JE, Jones MH, Gross B. NASA TN D-2396: Experimental determination of the dependence of crack extension force on crack length for a single-edge notch tension specimen. 1964.
- [4] ASTM E399-20: Standard Test Method for Linear-Elastic Plane-Strain Fracture Toughness of Metallic Materials. West Conshohocken, PA: ASTM International; 2020.
- [5] ASTM E1820-20: Standard Test Method for Measurement of Fracture Toughness. West Conshohocken, PA: ASTM International; 2020.
- [6] Zhu XK, Joyce JA. Review of fracture toughness ( $G$ ,  $K$ ,  $J$ , CTOD, CTOA) testing and standardization. Eng Fract Mech 2012;85:1–46. <https://doi.org/DOI> 10.1016/j.engfracmech.2012.02.001.
- [7] Dadfarnia M, Sofronis P, Somerday BP, Balch DK, Schembri P, Melcher R. On the environmental similitude for fracture in the SENT specimen and a cracked hydrogen gas pipeline. Eng Fract Mech 2011;78:2429–38. <https://doi.org/DOI> 10.1016/j.engfracmech.2011.06.002.
- [8] Zhu XK. Progress in development of fracture toughness test methods for SENT specimens. International Journal of Pressure Vessels and Piping 2017;156:40–58. <https://doi.org/10.1016/j.ijpvp.2017.07.004>.
- [9] Zhu XK. Review of fracture toughness test methods for ductile materials in low-constraint conditions. International Journal of Pressure Vessels and Piping 2016;139–140:173–83. <https://doi.org/10.1016/j.ijpvp.2016.02.006>.

- [10] Johnson HH. Calibrating the Electric Potential Method for Studying Slow Crack Growth. *Materials Research and Standards* 1965;5:442–5.
- [11] Schwalbe K-H, Hellmann D. Application of the Electrical Potential Method to Crack Length Measurements Using Johnson’s Formula. *J Test Eval* 1981;9:218–21.
- [12] Donald JK, Ruschau J. Direct current potential difference fatigue crack measurement techniques. In: Marsh KJ, Smith RA, Ritchie RO, editors. *Fatigue crack measurement: techniques and applications*, EMAS; 1991, p. 11–37.
- [13] Gangloff RP, Slavik DC, Piascik RS, Van Stone RH. Direct Current Electrical Potential Measurement of the Growth of Small Cracks. In: Larsen JM, Allison JE, editors. *Small-Crack Test Methods*, ASTM STP 1149, Philadelphia: American Society for Testing and Materials; 1992, p. 116–68.
- [14] Ritchie RO, Lankford J, editors. *Small Fatigue Cracks*. Warrendale, PA: TMS-AIME; 1986.
- [15] Gangloff RP, Ritchie RO. Environmental Effects Novel to the Propagation of Short Fatigue Cracks",. In: Bilby BA, Miller KJ, Willis JR, editors. *Fundamentals of Deformation and Fracture*, Cambridge, UK: Cambridge University Press; 1986, p. 529–58.
- [16] Gangloff RP. Crack size effects on the chemical driving force for aqueous corrosion fatigue. *Metallurgical Transactions A* 1985;16:953–69. <https://doi.org/10.1007/BF02814848>.
- [17] Gangloff RP. Ethylene Inhibition of Gaseous Hydrogen Embrittlement in High Strength Steel. In: Wei RP, Gangloff RP, editors. *ASTM STP 924: Basic Questions in Fatigue*, Volume 2, Philadelphia, PA: ASTM; 1988, p. 230–51.
- [18] Piascik RS, Gangloff RP. Environmental fatigue of an Al-Li-Cu alloy: part I. Intrinsic crack propagation kinetics in hydrogenous environments. *Metallurgical Transactions A* 1991;22:2415–28. <https://doi.org/10.1007/BF02665008>.
- [19] Warner JS, Gangloff RP. Molybdate inhibition of corrosion fatigue crack propagation in precipitation hardened Al-Cu-Li. *Corros Sci* 2012;62:11–21. <https://doi.org/DOI10.1016/j.corsci.2012.03.038>.
- [20] Warner JS, Kim S, Gangloff RP. Molybdate inhibition of environmental fatigue crack propagation in Al-Zn-Mg-Cu. *Int J Fatigue* 2009;31:1952–65.
- [21] Warner JS, Gangloff RP. Alloy induced inhibition of fatigue crack growth in age-hardenable Al-Cu Alloys. *Int J Fatigue* 2012;42:35–44. <https://doi.org/10.1016/j.ijfatigue.2011.04.013>.
- [22] Bray GH, Glazov M, Rioja RJ, Li D, Gangloff RP. Effect of artificial aging on the fatigue crack propagation resistance of 2000 series aluminum alloys. *Int J Fatigue* 2001;23:265–76. [https://doi.org/10.1016/S0142-1123\(01\)00159-1](https://doi.org/10.1016/S0142-1123(01)00159-1).
- [23] Burns JT, Bush RW, Ai JH, Jones JL, Lee Y, Gangloff RP. Effect of water vapor pressure on fatigue crack growth in Al-Zn-Cu-Mg over wide-range stress intensity factor loading. *Eng Fract Mech* 2015;137:34–55. <https://doi.org/10.1016/j.engfracmech.2014.11.009>.
- [24] Van Stone RH. Residual life prediction methods for gas turbine components. *Materials Science and Engineering: A* 1988;103:49–61. [https://doi.org/10.1016/0025-5416\(88\)90551-4](https://doi.org/10.1016/0025-5416(88)90551-4).
- [25] Gallagher J, Nicholas T, Gunderson A, Ruschau J, Miedlar P, Hutson A, et al. *AFRL-ML-WP-TR-2005-4102: Advanced High Cycle Fatigue Life Assurance Methodologies*, . Dayton, OH: 2004.

- [26] Crane CB, Gangloff RP. Stress corrosion cracking of Al-Mg alloy 5083 sensitized at low temperature. *Corrosion* 2016;72:221–41. <https://doi.org/10.5006/1766>.
- [27] Pioszak GL, Gangloff RP. Hydrogen Environment Assisted Cracking of a Modern Ultra-High Strength Martensitic Stainless Steel. *Corrosion* 2017;73:1132–56. <https://doi.org/10.5006/2437>.
- [28] Gangloff RP, Ha HM, Burns JT, Scully JR. Measurement and Modeling of Hydrogen Environment-Assisted Cracking in Monel K-500. *Metallurgical and Materials Transactions A* 2014;45:3814–34. <https://doi.org/10.1007/s11661-014-2324-z>.
- [29] Gangloff RP, Turnbull A. Crack Electrochemistry Modeling and Fracture Mechanics Measurement of the Hydrogen Embrittlement Threshold. In: Jones RH, Gerberich WW, editors. *Modeling Environmental Effects on Crack Initiation and Propagation*, Warrendale, PA: TMS-AIME; 1986, p. 55–81.
- [30] Gangloff RP. Probabilistic Fracture Mechanics Simulation of Stress Corrosion Cracking Using Accelerated Laboratory Testing and Multi-Scale Modeling. *Corrosion* 2016;72:862–80. <https://doi.org/10.5006/1920>.
- [31] Saxena A, Bassi F, Nibur K, Newman JC. On single-edge-crack tension specimens for tension-compression fatigue crack growth testing. *Eng Fract Mech* 2017;176:343–50. <https://doi.org/10.1016/j.engfracmech.2017.03.030>.
- [32] Narasimhachary SB, Bhachu KS, Shinde SR, Gravett PW, Newman JC. A single edge notch specimen for fatigue, creep-fatigue and thermo-mechanical fatigue crack growth testing. *Eng Fract Mech* 2018;199:760–72. <https://doi.org/10.1016/j.engfracmech.2017.08.011>.
- [33] Zhu XK. Full-range stress intensity factor solutions for clamped SENT specimens. *International Journal of Pressure Vessels and Piping* 2017;149:1–13. <https://doi.org/10.1016/j.ijpvp.2016.11.004>.
- [34] Slavik DC. Environmental Fatigue Crack Growth and Microscopic Damage Mechanisms in AA2090. Ph.D. Dissertation. University of Virginia, 1993.
- [35] Tada H, Paris P, Irwin G. *The Stress Analysis of Cracks Handbook*. St. Louis, MO: Paris Productions Incorporated; 1985.
- [36] Tokuda N, Yamamoto Y. Accurate Determination of Stress Intensity Factors in Cracked Plates. *Journal of the Society of Naval Architects of Japan* 1972;132:349–60. [https://doi.org/10.2534/jjasnaoe1968.1972.132\\_349](https://doi.org/10.2534/jjasnaoe1968.1972.132_349).
- [37] Joyce J, Hackett E, Roe C. Effects of Crack Depth and Mode of Loading on the J-R Curve Behavior of a High-Strength Steel. In: Hackett EM, Schwalbe K-H, Dodds RH, editors. *Constraint Effects in Fracture*, West Conshohocken, PA: ASTM International; 1993, p. 239–63. <https://doi.org/10.1520/STP18031S>.
- [38] Hammond MJ, Fawaz SA. Stress intensity factors of various size single edge-cracked tension specimens: A review and new solutions. *Eng Fract Mech* 2016;153:25–34. <https://doi.org/10.1016/j.engfracmech.2015.12.022>.
- [39] Gross B, Srawley JE, Brown Jr. WF. NASA TN D-2395: Stress intensity factors for a single-edge-notch tension specimen by boundary collocation of a stress function. 1964.
- [40] Sanford RJ, Kirk MT. A comparison of boundary and global collocation solutions for K and CMOD calibration functions. *Exp Mech* 1991;31:52–9. <https://doi.org/10.1007/BF02325724>.
- [41] Wang W-C, Chen T-L. Half-fringe photoelastic determination of opening mode stress intensity factor for edge cracked strips. *Eng Fract Mech* 1989;32:111–22.

- [42] Bowie OL. Rectangular tensile sheet with symmetric edge cracks. J Appl Mech 1964;32:208–12. <https://doi.org/10.1115/1.3629588>.
- [43] Bowie OL, Neal DM. Single edge cracks in rectangular tensile sheet. J Appl Mech 1965;32:708–9. <https://doi.org/10.1115/1.3627290>.
- [44] Emery AF, Walker Jr. GE, Williams JA. A Green's function for the stress-intensity factors of edge cracks and its application to thermal stresses. Journal of Basic Engineering 1969;91:618–24.
- [45] Jack AR. Stress intensity factors for an edge notched tension specimen with restrained ends. Engineering Fracture Mechanics 1971;3:349–50.
- [46] Pook LP. The effect of friction on pin jointed single edge notch fracture toughness test specimens. International Journal of Fracture Mechanics 1968;4:295–7. <https://doi.org/10.1007/BF00185265>.
- [47] Wan KC, Chen GS, Gao M, Wei RP. On the conventional K calibration equations for single-edge-cracked tension specimens. Eng Fract Mech 1996;54:301–5. [https://doi.org/10.1016/0013-7944\(95\)00185-9](https://doi.org/10.1016/0013-7944(95)00185-9).
- [48] Ciccone MP. The Effect of Corrosion Product Formation on Fatigue Crack Closure of AA7075-T6511 and AA7055-T74511. University of Virginia, 2005.
- [49] Thomas RLS, Scully JR, Gangloff RP. Internal hydrogen embrittlement of ultrahigh-strength AERMET 100 steel. Metallurgical and Materials Transactions A 2003;34:327–44. <https://doi.org/10.1007/s11661-003-0334-3>.
- [50] Galyon Dorman SE, Fawaz SA. Examination of the effects of specimen geometry on single edge-cracked tension specimens. Eng Fract Mech 2019;209:221–7. <https://doi.org/10.1016/j.engfracmech.2019.01.028>.
- [51] Galyon Dorman SE, Rausch JW, Arunachalam SR, Burns JT, Gangloff RP, Fawaz SA. SAFE-RPT-16-045: Managing Environmental Impacts on Time-Cycle Dependent Structural Integrity of High Performance DoD Alloys. Colorado Springs, CO: 2016.
- [52] Shoemaker TK, Harris ZD, Burns JT. Comparing Stress Corrosion Cracking Behavior of Additively Manufactured and Wrought 17-4PH Stainless Steel. Corrosion 2022;78:528–46. <https://doi.org/10.5006/4064>.
- [53] Pioszak GL, Gangloff RP. Hydrogen Environment Assisted Cracking of Modern Ultra-High Strength Martensitic Steels. Metall Mater Trans A Phys Metall Mater Sci 2017;48:4025–45. <https://doi.org/10.1007/s11661-017-4156-0>.
- [54] Harris ZD, Burns JT. The Effect of Loading Rate on the Environment-Assisted Cracking Behavior of AA7075-T651 in Aqueous NaCl Solution. Corrosion and Materials Degradation 2021;2:360–75. <https://doi.org/10.3390/cmd2030019>.
- [55] McMahon ME, Steiner PJ, Lass AB, Burns JT. The effect of temper and composition on the stress corrosion cracking of Al-Mg alloys. Corrosion 2017;73:347–61. <https://doi.org/10.5006/2317>.
- [56] Somerday BP, Young LM, Gangloff RP. Crack tip mechanics effects on environment-assisted cracking of beta-titanium alloys in aqueous NaCl. Fatigue Fract Eng Mater Struct 2000;23:39–58. <https://doi.org/10.1046/j.1460-2695.2000.00243.x>.
- [57] E647-15e1. Standard Test Method for Measurement of Fatigue Crack Growth Rates. ASTM Book of Standards 2016:1–49. <https://doi.org/10.1520/E0647-15E01.2>.
- [58] ABAQUS/Standard 2021 n.d.
- [59] Fracture Analysis Code (versions 7.4, 7.5) n.d.

- [60] Banks-Sills L, Hershkovitz I, Wawrzynek PA, Eliasi R, Ingraffea AR. Methods for calculating stress intensity factors in anisotropic materials: Part I— $z=0$  is a symmetric plane. *Eng Fract Mech* 2005;72:2328–58. <https://doi.org/10.1016/j.engfracmech.2004.12.007>.
- [61] Harris ZD, Dubas EM, Schrock DJ, Locke JS (Warner), Burns JT. Assessing the fatigue crack growth behavior of highly sensitized AA5456-H116 under cathodic polarization. *Materials Science and Engineering: A* 2020:139792. <https://doi.org/10.1016/j.msea.2020.139792>.
- [62] Clark W, Hudak S. Variability in Fatigue Crack Growth Rate Testing. *J Test Eval* 1975;3:454–76. <https://doi.org/10.1520/JTE11702J>.
- [63] Anderson TL. *Fracture Mechanics: Fundamentals and Applications*. 3rd ed. Taylor & Francis; 2005.
- [64] Hudak Jr. SJ, Bucci RJ, editors. *ASTM STP 738: Fatigue Crack Growth Measurement and Data Analysis*. Philadelphia, PA: ASTM; 1981.
- [65] Suresh S. *Fatigue of materials*. 2nd ed. Cambridge, UK: Cambridge University Press; 1998.
- [66] Pippin R, Hohenwarter A. Fatigue crack closure: a review of the physical phenomena. *Fatigue Fract Eng Mater Struct* 2017;40:471–95. <https://doi.org/10.1111/ffe.12578>.
- [67] Hutchinson JW. Singular behaviour at the end of a tensile crack in a hardening material. *J Mech Phys Solids* 1968;16:13–31.
- [68] Rice JR, Rosengren GF. Plane strain deformation near a crack tip in a power-law hardening materials. *J Mech Phys Solids* 1968;16:1–12.
- [69] John R, Rigling B. Effect of height to width ratio on K and CMOD solutions for a single edge cracked geometry with clamped ends. *Eng Fract Mech* 1998;60:147–56. [https://doi.org/10.1016/S0013-7944\(98\)00009-5](https://doi.org/10.1016/S0013-7944(98)00009-5).
- [70] Van Stone RH. Private Communication 2023.
- [71] Bomarito GF, Townsend T, Hochhalter JD, Adams E, Esham K, Vera D. BINGO 2018. <https://github.com/nasa/bingo>.
- [72] Galyon Dorman SE, Niebuhr JH, Locke JS, Free B. Paper No. 2019-0218-0314-000077: The Development of a Method for Complex Environment Corrosion Fatigue Testing. 2019 DoD-Allied Nations Technical Corrosion Conference, 2019.
- [73] McMahon ME, Harris ZD, Scully JR, Burns JT. The effect of electrode potential on stress corrosion cracking in highly sensitized Al–Mg alloys. *Materials Science and Engineering: A* 2019;767:138399. <https://doi.org/10.1016/j.msea.2019.138399>.
- [74] Crane CB, Kelly RG, Gangloff RP. Crack chemistry control of intergranular stress corrosion cracking in sensitized Al-Mg. *Corrosion* 2016;72:242–63. <https://doi.org/10.5006/1852>.
- [75] Burns JT, Harris ZD, Dolph JD, Gangloff RP. Measurement and Modeling of Hydrogen Environment Assisted Cracking in a Ni-Cu-Al-Ti Superalloy. *Metallurgical and Materials Transactions A* 2016;47:990–7. <https://doi.org/10.1007/s11661-015-3315-4>.
- [76] Harris ZD, Dolph JD, Pioszak GL, Rincon Troconis BC, Scully JR, Burns JT. The Effect of Microstructural Variation on the Hydrogen Environment-Assisted Cracking of Monel K-500. *Metallurgical and Materials Transactions A* 2016;47:3488–510. <https://doi.org/10.1007/s11661-016-3486-7>.

- [77] Harris ZD, Burns JT. The effect of isothermal heat treatment on hydrogen environment-assisted cracking susceptibility in Monel K-500. *Materials Science and Engineering: A* 2019;764:138249. <https://doi.org/10.1016/j.msea.2019.138249>.
- [78] Harris ZD, Dubas EM, Popernack AS, Somerday BP, Burns JT. Elucidating the loading rate dependence of hydrogen environment-assisted cracking in a Ni-Cu superalloy. *Theoretical and Applied Fracture Mechanics* 2021;111:102846. <https://doi.org/10.1016/j.tafmec.2020.102846>.
- [79] Harris ZD, Guiseva K, Scully JR, Burns JT. On the hydrogen environment-assisted cracking resistance of a compositionally complex Co–Ni–Cr–Fe–Mo–Ti alloy. *Materials Science and Engineering: A* 2020;802:140601. <https://doi.org/10.1016/j.msea.2020.140601>.
- [80] Harris ZD, Burns JT. On the loading rate dependence of environment-assisted cracking in sensitized AA5456-H116 exposed to marine environments. *Corros Sci* 2022;201:110267. <https://doi.org/10.1016/j.corsci.2022.110267>.
- [81] Steiner P, Harris Z, Vicente Moraes C, Kelly R, Burns J. Investigation of IG-SCC growth kinetics in Al-Mg alloys in thin film environments. *Corrosion* 2021. <https://doi.org/10.5006/3833>.
- [82] McMahon ME, Steiner PJ, Lass AB, Burns JT. The effect of loading orientation on the stress corrosion cracking of Al-Mg alloys. *Corrosion* 2017;73:713–23. <https://doi.org/10.5006/2343>.
- [83] Harris ZD, Marshall RS, Kelly RG, Burns JT. Coupling fracture mechanics experiments and electrochemical modeling to mitigate environment-assisted cracking in engineering components. *Corrosion* 2023;79:363–75.